High Temperature Gas Sensor for Coal Combustion System

Award Number: DE-FE-31564

Project Title: High Temperature Gas Sensor for Coal Combustion System

Principal Investigator: Dr. Xingbo Liu
(304) 293-3339
Xingbo.Liu@mail.wvu.edu

Project Period: March 1,2018 to August 31, 2020

Recipient Organization: West Virginia University

Submission Date: **December 9, 2020**

DUNS Number: 929332658

Recipient Organization (Name and Address): West Virginia University
Morgantown, West Virginia 26506

Project/Grant Period (Start Date, End Date): 03/01/2018 to 8/31/2020

Reporting Period End Date: August 31, 2020

Report Term or Frequency: Final Technical Report

Signature of Submitting Official (electronic signatures (i.e., Adobe Acrobat) are acceptable)

Executive Summary

Robust gas sensors that offer real-time feedback about combustion in coal-fired power plants promise greater energy efficiency with fewer harmful emissions while also improving the bottom line for power generators. Currently, no technology meets this objective. Therefore, the objectives of this project are to develop an accurate, robust, reliable, high temperature sensor offering near real-time feedback to plant operators using a novel catalytic/non-catalytic sensor design to detect target gases available for oxidization. Such a sensor would inform power plant operators how to adjust the amount of fuel and air for an optimal performance.

During the 2-year project funded by National Energy Technology Laboratory, the research team, headed by WVU, includes scientists and engineers from Los Alamos National Laboratory, KWJ Engineering, and Longview Power, LLC, have developed a robust high temperature CO sensor offers the best sensitivity, selectivity, and stability in the published literature.

Three materials, $La_{0.8}Sr_{0.2}CrO_3$ (LSCr) perovskite, metallic Pd-Au and nickel oxide (NiO) have been systematically studied for their feasibility of being an in-situ high-temperature CO gas sensor for coal combustion system. LSCr and Pd-Au exhibits promising performance to CO sensing below 900 ºC. However, when the temperature reaches to 1000 ºC, only NiO is demonstrating excellent sensitivity, selectivity and stability.

Under the conditions of 0.5%-3% O_2 and 1000ºC, the fabricated YSZ-based mixed potential sensor using porous NiO shows good sensitivity to ppm-scale CO, even having as high as 36 mV response to 1000 ppm CO. The effect of gas transport of sample gas, geometry and structure of NiO electrode was studied. Results show that a better gas transport is much beneficial to an improved sensitivity. NiO with porous structure is much more sensitive to CO than that with dense structure, but the 90% response time is much higher due to the slow gas diffusion. Selectivity tests on how CO_2, CH_4 and steam affect CO sensing were also demonstrated. It's worth noting that the potential of NiO exhibits positive relationship with CO content. We found it might be due to the electrochemical reduction of CO during the interaction with NiO at 1000 ºC rather than being oxidized.

Finally, because of the great potential of our NiO electrode, we managed to incorporate this sensor into a novel sensor test station in the coal-fired boiler at Longview Power LLC., Longview operates one the U.S.'s newest and cleanest coal-fired boilers, an Amec Foster Wheeler first-of-a-kind, once-through, low-mass flux, vertical tube Advanced Supercritical Boiler producing 700 MW of electricity. Our testing results shows the effectiveness of our gas sensor to provide real-time CO and O2 sensing, and the need to improve the sensor packaging & accessories to improve the long-term stability in real operation conditions.

Table of Contents

List of Figures

600, and 900ppm of CO. The negligible voltage produced by this device in lean conditions shows that the electrodes generate identical voltages to the CO/O_2 mixture at 700°C.

Figure 16. SEM image of a high surface area Pt ink (cat. no. 5570) acquired from ESL ElectroScience, final firing condition was 1100°C for 18h.

Figure 17. Sensor response of a Pd-Au/Pt//YSZ//Pt electrochemical button cell upon exposure to 250 and 500ppm CO in a background of 2.5%O_2/5% CO_2/50% RH. The voltage is measure between WE and CE.

Figure 18. Sensor response of a Pd-Au/Pt//YSZ//Pt electrochemical button cell upon exposure to 250, 500, 750, 1000, 1250, and 1500 ppm CO in a background of 2.5%O_2/5% CO_2/50% RH after 3 day anneal at 900°C.

Figure 19. Sensor response of a Pd-Au/Pt//YSZ//Pt electrochemical button cell upon exposure to 100, 250, 500, 750, and 1000 ppm CO in a background of 2.5%O_2/5% CO_2/50% RH after 3 day anneal at 900°C.

Figure 20 The FluePt-RefPt signal of a PdAu-based sensor sample to the changing ppm CO in two-chamber design in a background of 2% O2 and balanced N_2 at 900°C.

Figure. 21 The PdAu-RefPt signal of a PdAu-based sensor sample to the changing ppm CO in two-chamber design in a background of 2% O2 and balanced N_2 at 900°C.

Figure. 22 The PdAu-RefPt signal of a PdAu-based sensor sample to the changing ppm CO in two-chamber design in a background of 2% O2 and balanced N_2 at 900°C.

Figure. 23 (a) Schematic illustration of three electrodes in the sensor sample, and the voltage difference between each two electrodes was recorded. (b) The three signals variations with the changing CO concentration in the P_{O2} = 2.1% and 1000 ºC. The flow rate of the simulated flue gas was fixed to 200 sccm; the flow rate of air is 100 sccm in the reference side.

Figure. 24 Signals responding to the changing CO concentration in the P_{O2} = 2.1% and 1000 ºC. (a) PtRef-PtFlue and (b) PtFlue-NiO. The simulative flue gas is composed of ppm CO, N_2 and O_2. The flow rate of the simulative flue gas is 200 sccm.

Figure. 25 (a) The three signals recorded in the P_{O2} = 1.05% and 1000 ºC with the changing CO concentration from 0 ppm to 1000 ppm. (b) Magnified illustration of the signal PtFlue-NiO. The simulative flue gas is composed of ppm CO, N_2 and O_2.

Figure. 26 (a) The three signals recorded in the P_{O2} = 0.5% and 1000 ºC with the changing CO concentration from 0 ppm to 1000 ppm. (b) Magnified illustration of the signal PtFlue-NiO. The simulative flue gas is composed of ppm CO, N_2 and O_2.

Figure 27 demonstration of the sensing behavior of the developed sensor sample to the CO concentration ranging from 1000 ppm – 100 ppm – 1000 ppm under 1% PO_2, 2% PO_2 and 3% PO_2 at 1000 ºC

Figure 28 The sensing performance of the porous NiO to the ppm CO variation under 1%-3% O_2 and 900-1000 ºC.

Figure 29 the sensing performance of the dense NiO to the ppm CO variation under 1%-3% O_2 and 900-1000 ºC.

Figure 30 The effect of CO_2 on the sensing performance of CO

List of tables

1. Milestone Status Report

Milestone Number	Assoc. SOPO Task(s)	Title/ Description	Planned Completion Date	Actual Completion Date	Percent Completed	Verification Method	Comments
1.0		Project Management	08/31/2020		100%	Preparation and publication of reports, project meetings and tracking project milestones	Quarterly report was generated
2.0		Sensor Development	09/30/2019		100%	Macrographs of sensor samples, microstructure of sensor electrodes and data collected	
3.0		Sensor Packaging	09/30/2019		100%	Images of testing set-up and data collected	
4.0		Lab-scale Sensor Testing	12/31/2019		100%	Collected Data and illustrations	
5.0		Post-mortem Characterization	02/29/2020		100%	Microstructure of sensor samples	
6.0		Electrochemical Mechanism Investigation	08/31/2020		100%	Explanation of data in the reports	
7.0		Sensor Testing in Utility Boiler	2/29/2020		100%		

2 Major Accomplishments

Task 1.0 Project Management and Planning

The project management plan was submitted after the award. All work elements required to maintain and revise the project management plan were finished and all activities in accordance with the plan were managed and reported. The principle investigator kept in communication with DOE/NETL and other project participants with any changes or deviations from the agreed upon plan. All quarterly reports were submitted within a timely manner and the PI tracked project tasks against the project timeline and the project management plan to ensure that milestones and go-no go decision points were being met. All project tasks, milestones and decision points have been completed and passed.

The principle investigator kept in communication with the project officer at NETL and our partners Los Alamos National Lab and KWJ Engineering about the status of the project, any issues regarding the project, and concerns about the timeline. The PI also gave tours throughout the project to the project officer and other partners to keep them up to date on the status of the project and the laboratory testing.

Task 2.0 High Temperature Gas Sensor Development

Three candidate materials were systematically examined which are La-Sr-Cr-O perovskite (LSCr), PdAu and nickel oxide (NiO). Among the three sensing materials, all shows promising performance to CO sensing below 900 ºC, however, when the temperature reaches to 1000 ºC, NiO is exhibiting excellent sensitivity, selectivity and stability. The three sensor designs investigated are presented as follow.

1. A stick-shape sensor using LSCr perovskite as the sensing material

As seen in Fig. 1, the LSCr perovskite stick type of sensor consists of the top $La_{0.8}Sr_{0.2}CrO_3$ electrode, bottom dense Pt electrode, yttria-stabilized zirconium oxide tape electrolyte. On the reverse side which is not shown is the resistive Pt heater.

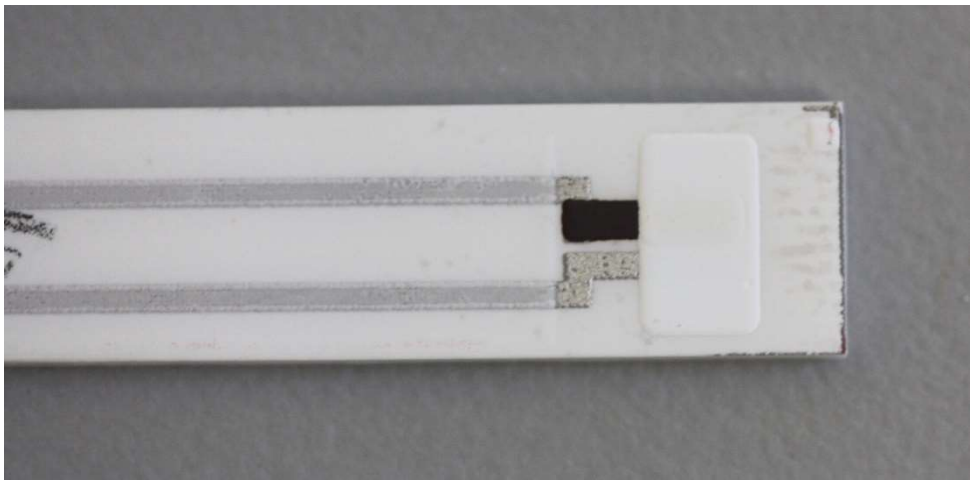

Figure 1. The stick-shape mixed-potential based electrochemical sensor used for rapid response screening (June – Sept. 2018) to CO up to 1050°C. Top electrode: La0.8Sr0.2CrO3. Bottom

electrode: dense Pt. Electrolyte: yttria-stabilzed zirconium oxide tape. Not shown: reverse side, resistive Pt heater not used for this work.

2. A Disk sensor pellet using metallic Pd-Au as sensing material

Three-electrode button cells were fabricated to test the low surface area Pd-Au alloy working electrode (WE) with a high surface area Pt counter electrode (CE) and reference electrode (RE) electrodes. The 3-terminal approach permits measurement of voltages versus an independent air reference electrode. A dense Pt ring was incorporated to permit forming a gas-tight seal via hydrogen brazing should these be field tested. The schematic illustration and the photograph of the sensing side of the PdAu-based sensor are shown in Fig. 2.

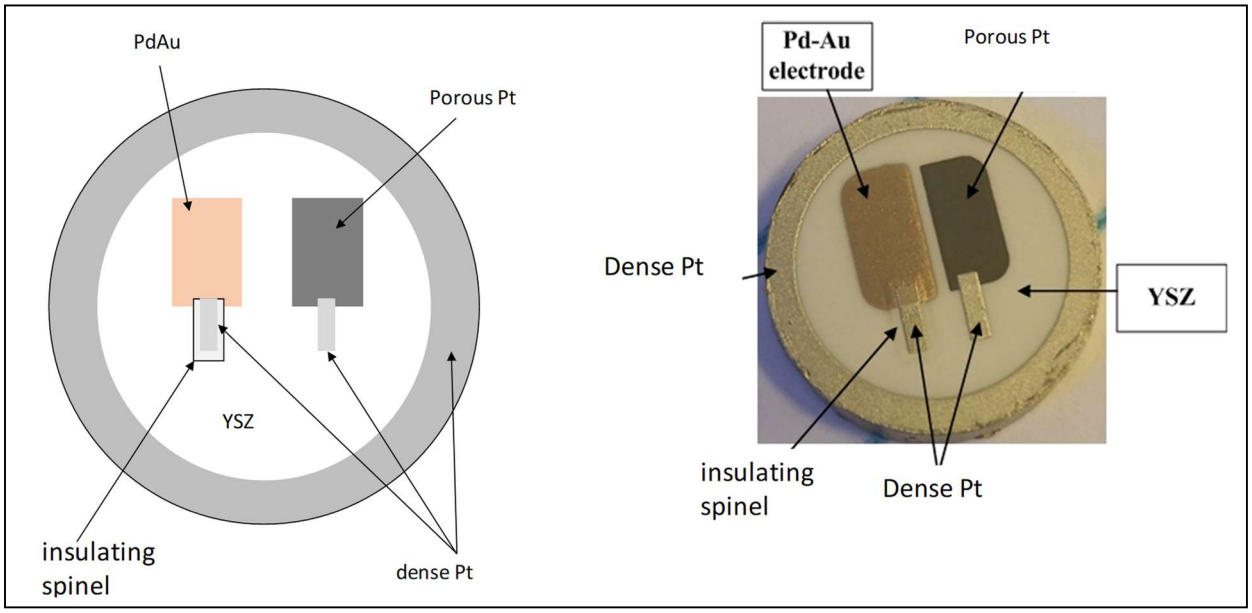

Figure 2. The schematic illustration and the photograph of the sensing side of the PdAu-based sensor.

3. A disk sensor pellet using Nickel oxide (NiO) as sensing material

Because NiO has been showing consistently great sensing performance during the period of the project, varied parameters concerning NiO sensor were considered, leading to different types of sensor designs.

One sensor design that was used is a YSZ-based disk pellet sensor with a pure and dense NiO sensing electrode as shown in Fig. 3 and Fig. 4. Fig. 3 is the schematic illustration; and Fig. 4 is the photographs. The sample pellet is YSZ-supported. On the flue/sensing side, a dense NiO electrode and a porous Pt electrode were fabricated, with a porous gold coated on the electrode surfaces as the current collector. On the air/reference side, Pt reference electrode was sintered on the YSZ surface and gold mesh was used as current collector.

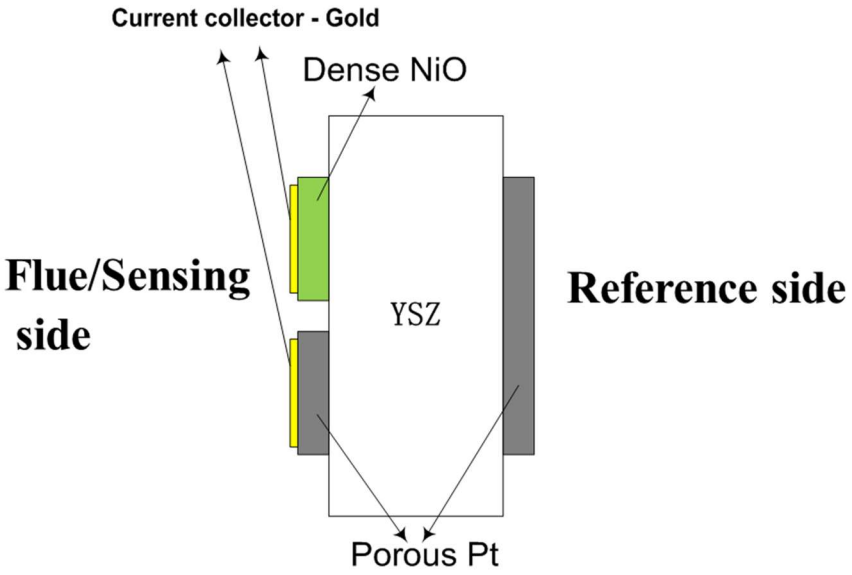

Figure. 3 Schematic illustration of the CO gas sensor sample. The flue gas/sensing side contains a dense NiO electrode and a porous Pt electrode with gold current collector. The reference electrode is porous Pt exposed to air, with a gold mesh as the current collector.

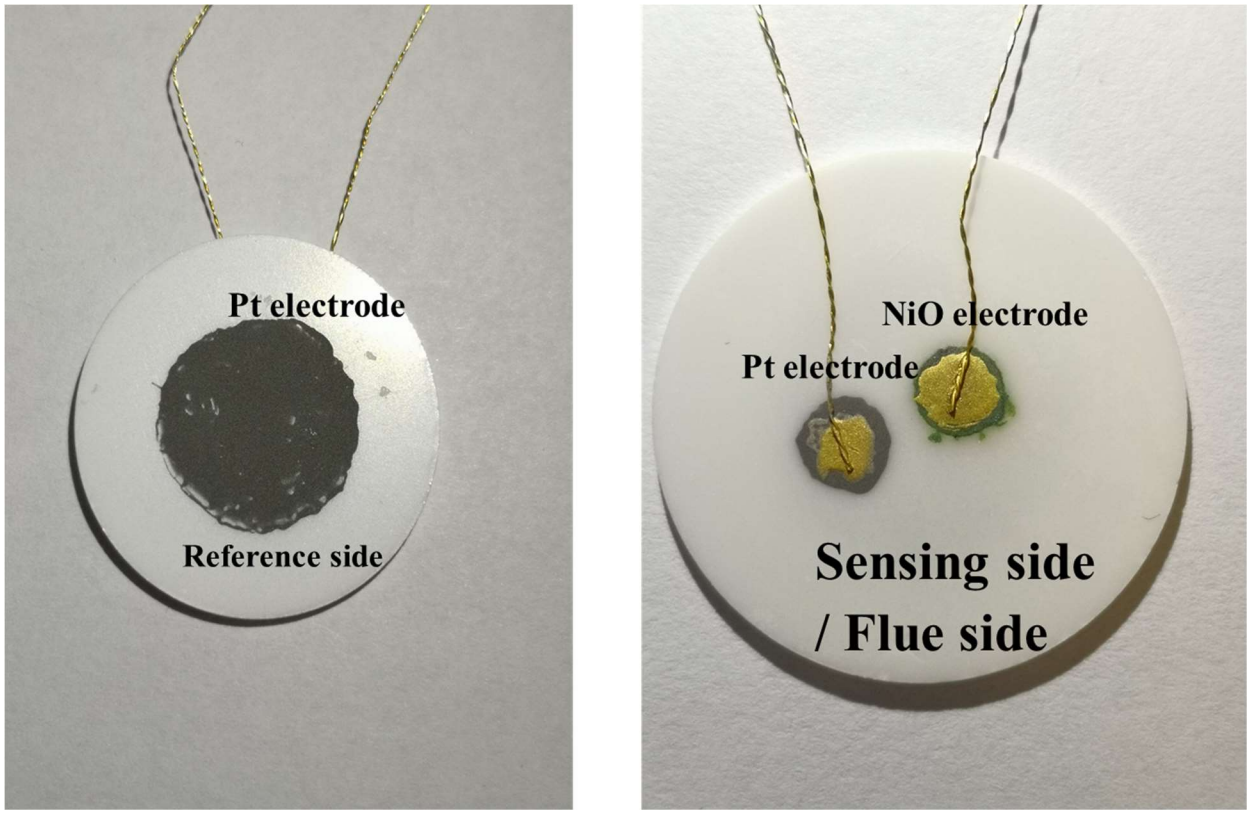

Figure. 4 Photographs of top views of the sensor sample, corresponding to Fig. 3.

To further explore the morphology's effects on the sensing behavior, another design, as shown in Fig. 5, was used which used dense NiO to compare with the porous NiO electrode. The flue

gas/sensing side contains a dense NiO electrode and a porous NiO electrode to testify the influence of morphology. The reference electrode is porous Pt exposed to air.

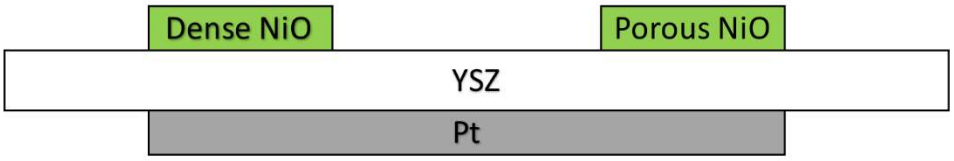

Fig. 5 Schematic illustration of sensor design using dense and porous NiO electrodes.

Resistive-type sensor using YSZ and NiO was also studied as presented in Fig. 6. In the sensing side, there are two porous NiO films sintered at the identical conditions (1400 oC for 4 hours). One is circle film working as the sensing electrode for mix-potential-type sensor design. The other is the stripe film for the resistive-type sensor design. The reference side is the porous Pt electrode exposed to air. Gold paste is used as current collector and gold wires is used for connection.

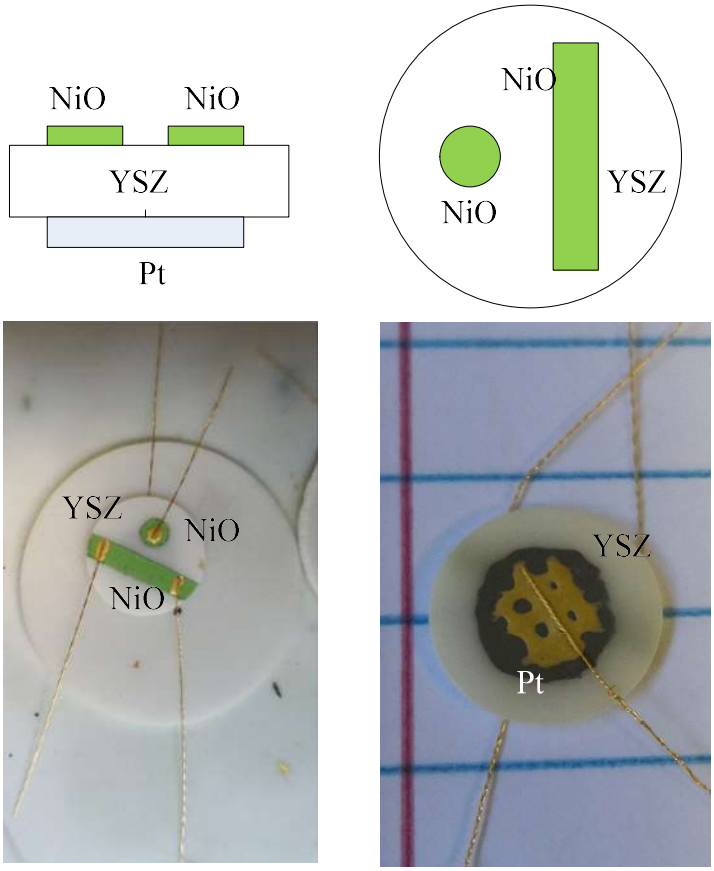

Figure 6 Schematic illustration and images of the sensor design that incorporated both the potential type and the resistive type.

At last, a simpler however more effective sensor design is developed, as seen in Fig. 7. In the sensing side, there is a porous NiO films sintered at 1400 ºC for 4 hours. The reference side is the porous Pt electrode exposed to air, sintered at 1400 ºC for 4 hours as well. The substrate is YSZ functioning as the electrolyte for oxygen transport.

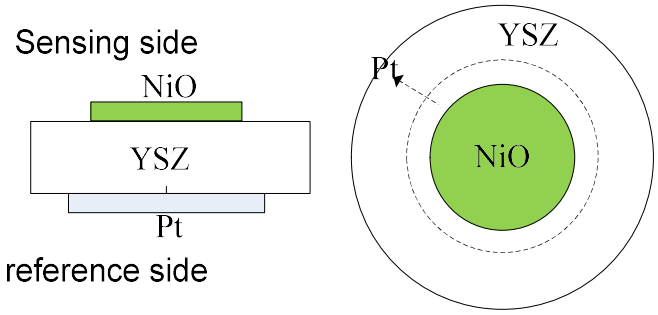

Figure 7 Schematic illustration of the sensor design that used porous NiO as sensing electrode.

Task 3.0 High Temperature Gas Sensor Electronics and Packaging

Based on different types of sensor designs, varied methods of packaging were used as well.
Fig. 8 shows photo graphs of a disassembled commercially available oxygen probe designed for heavy boiler/coal fired flue gas operation. As can be seen in the photographs, the oxygen electrochemical cell (Pt_{WE}//YSZ//Pt_{REF}) is brazed into stainless steel holder that is bolted to a stainless-steel process probe. The brazing creates a gas-tight seal that will not degrade with temperature cycling since the seal is made using a malleable metal such as gold. The removable sample cell permits easy replacement of the cell as the flue gas ages and deteriorates the sensor. A metal gasket is used to seal a form a gas tight boundary between reference gas (air) and the process gas despite a removable sample cell. A spring-loaded ceramic rod presses a current collector against the reference electrode while the WE signal is measured from the stainless-steel probe housing. A porous frit covers the inlet to the WE electrode to protect the sensor from particulate impingement. Fig. 9 is a simplified, summary schematic of this design.

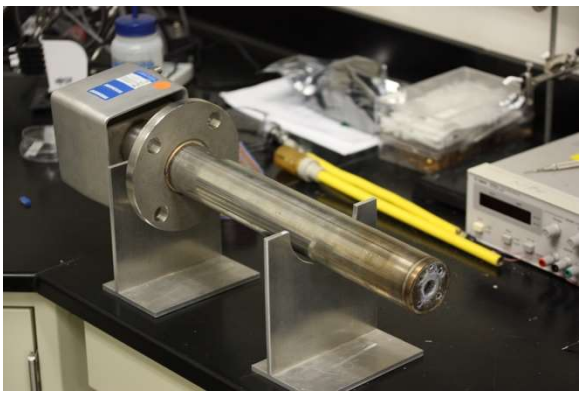

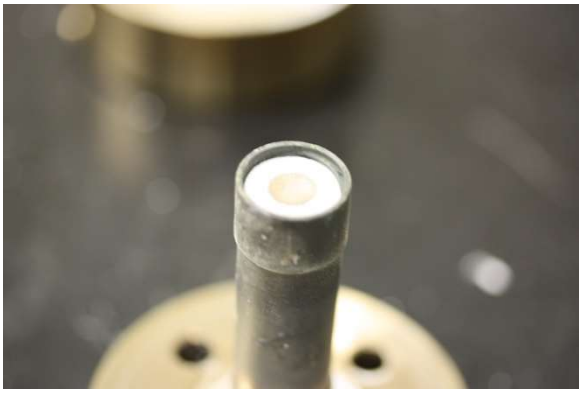

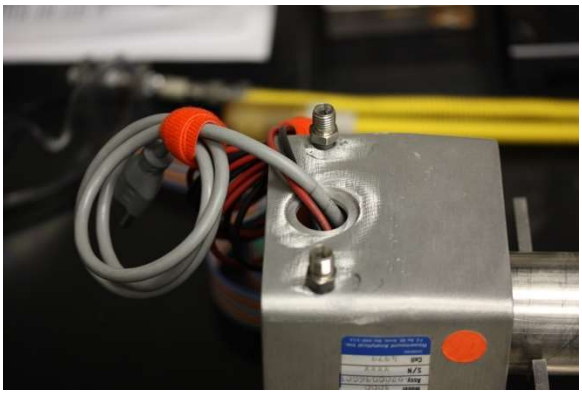

Figure 8: (upper left) Overall view of the process probe of length determined by boiler application. (upper right) The electrochemical cell, metal gasket and protective porous cap. (center left) Photograph of the reference electrode side of the YSZ-based oxygen cell. (center right) Looking down the bore axis of the process probe showing ceramic rod that picks up signal from the reference electrode. The interior volume is swept continuously with reference gas (air) to fixed oxygen chemical potential at the reference electrode. (lower left) gas fittings showing air reference access to the process probe.

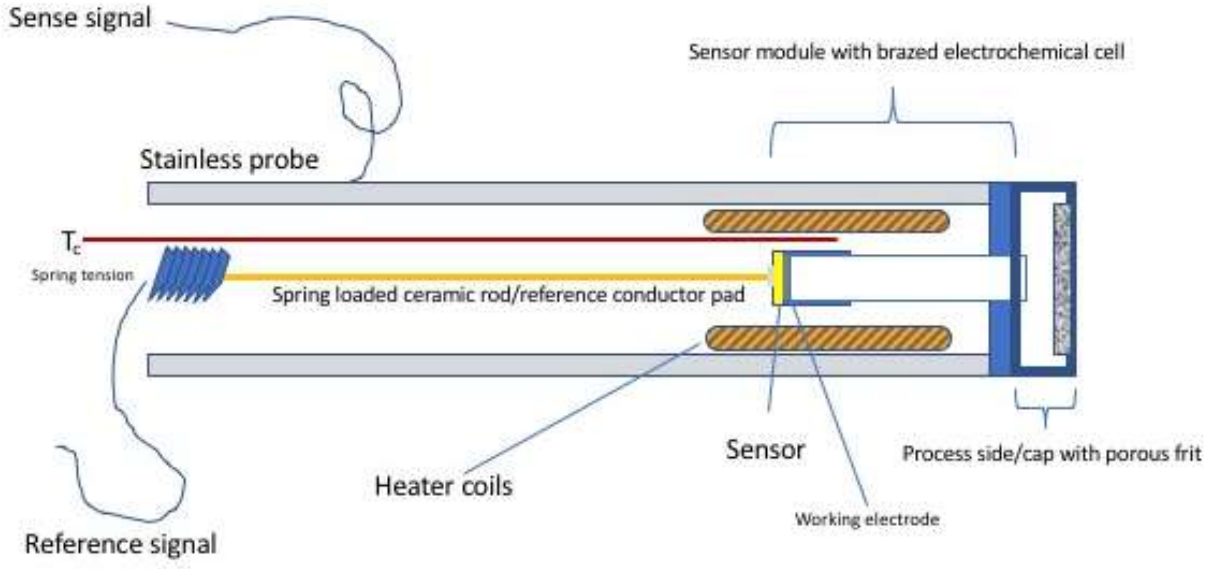

Figure 9: Schematic of the commercial oxygen combustion probe design.

The two-chamber lab-scale testing packaging setups are shown in Fig. 10 and Fig. 11. Both packaging methods worked greatly for lab-scale sensing test. The only difference is that Fig. 11 setup is more convenient than that of Fig. 10. For the packaging in Fig.10, the two gas compartments were made by using two SiO_2 tubes pressing against the sensor pellet; mica O-rings were positioned between SiO_2 tubes and the sensor pellet to obtain a good sealing. The volumes of the chambers are not large, which facilitates a fast atmosphere change in testing. In the flue/sensing side, two stainless steel tubes were flowed with two gases: one is ppm CO gas balanced with N_2, the other one is the air and N_2 mixture. In the region near the sensor, the two gas tubes were welded together for the final gas mixing to obtain the simulative flue gas. The composition of the simulative flue gas was controlled by mass controllers. There was 3 cm for gas mixing in the tube, and 1 cm for the mixed gas from the tube to contact the sensing electrodes. For the packaging in Fig.11, the air chamber is flowed through by 100 sccm air. The Pt electrode is exposed to the air chamber and functions as the reference electrode. The 200 sccm simulated flue gas containing ppm CO, air and N_2 is flowed into the flue gas chamber. The potentials between the NiO electrode and Pt reference electrode is monitored as the sensing signal of the mixed-potential type.

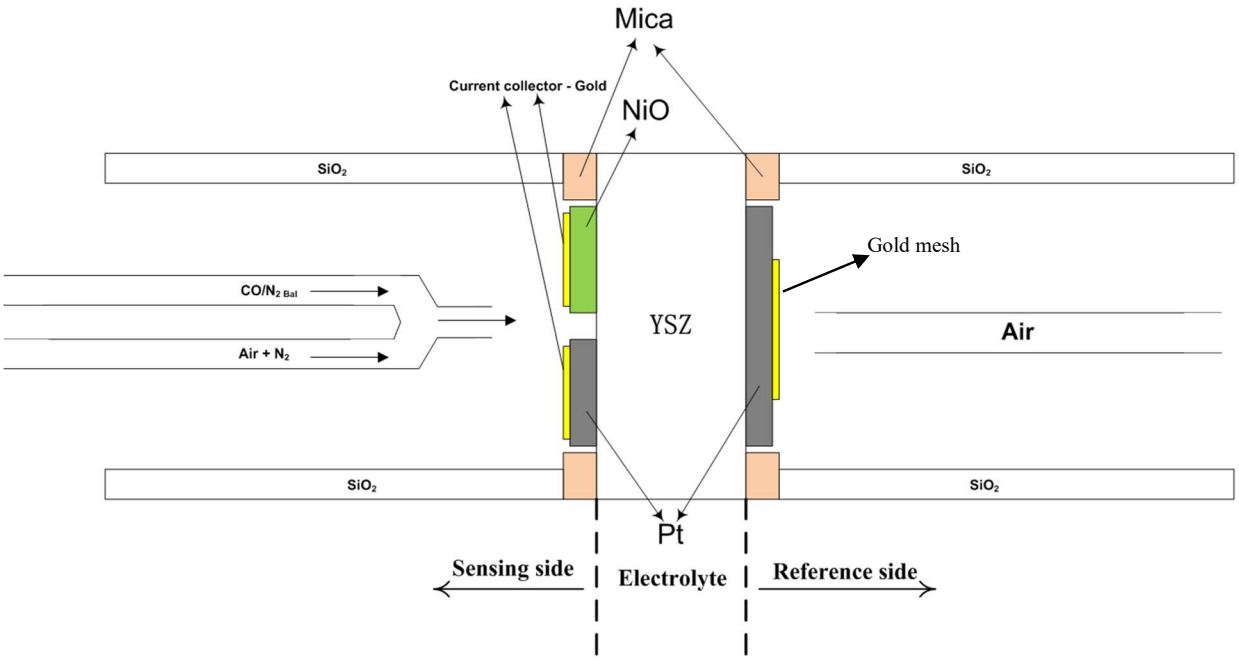

Figure. 10 Schematic illustration of the first two-chamber packaging sensor testing system.

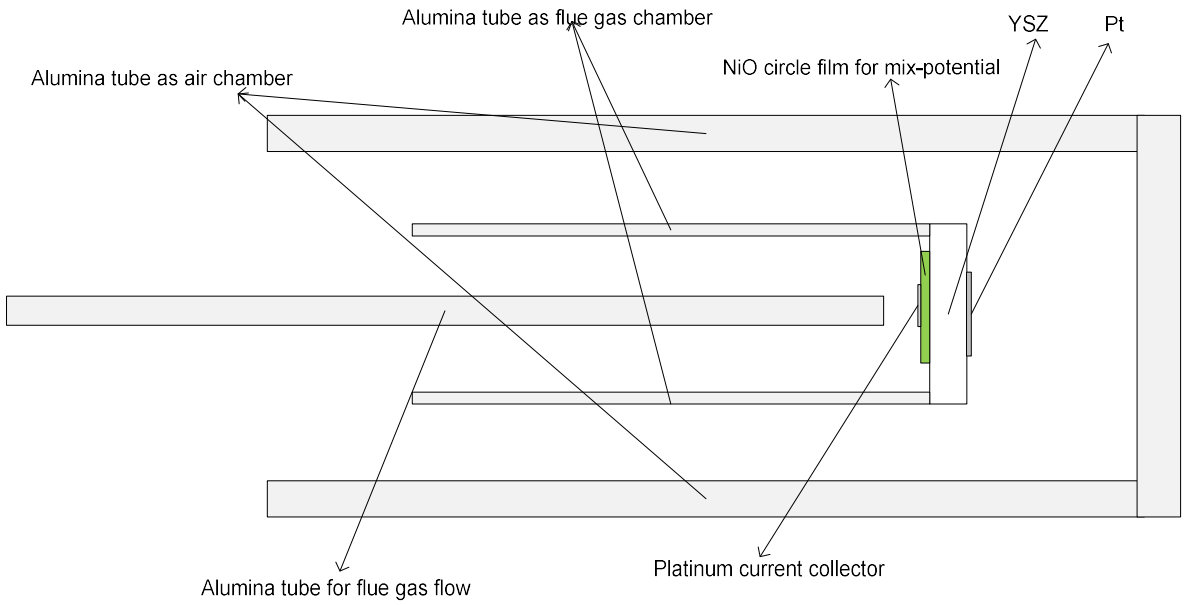

Figure 11 Schematic illustration of the testing system for the mixed-potential-type NiO-based sensor design.

Task 4.0 Lab-Scale Sensor Testing

Since we have examined three sensing materials, which are LSCr, Pd-Au and NiO, the testing results and discussions are presented by 3 subsections.

1. LSCr

Fig. 12 shows the response of the sensor at 700°C to 0, 300, 600, and 900ppm CO as PO_2 was decreased from 1% to less than 0.01% (N_2 balance). Since the stick sensors do not have an independent reference electrode with fixed oxygen potential, the voltages measured here reflect the difference in rates of electro catalysis and oxygen reduction kinetics between the two electrode materials and morphology that influence this voltage. Fig. 12 shows at 700°C, both electrodes exhibit identical kinetics with respect to CO oxidation until the PO_2 is reduced and rich-burn conditions are achieved. The large sensor response measured around the stoichiometry point is a well-known phenomenon of YSZ-based mixed potential sensors operated with an excess concentration of oxidizable gas species and is primarily driven by the Pt electrode (as evidenced here by the strong negative voltage). What is important for this project is that in lean conditions, there is essentially no voltage measured between the two electrodes for all CO concentrations tested. Increasing the sensor temperature to 900°C increased the voltage to CO at all concentrations at low PO2 however the negative voltage produced suggests that the Pt electrode is responsible not the La0.8Sr0.2SrO3 working electrode.

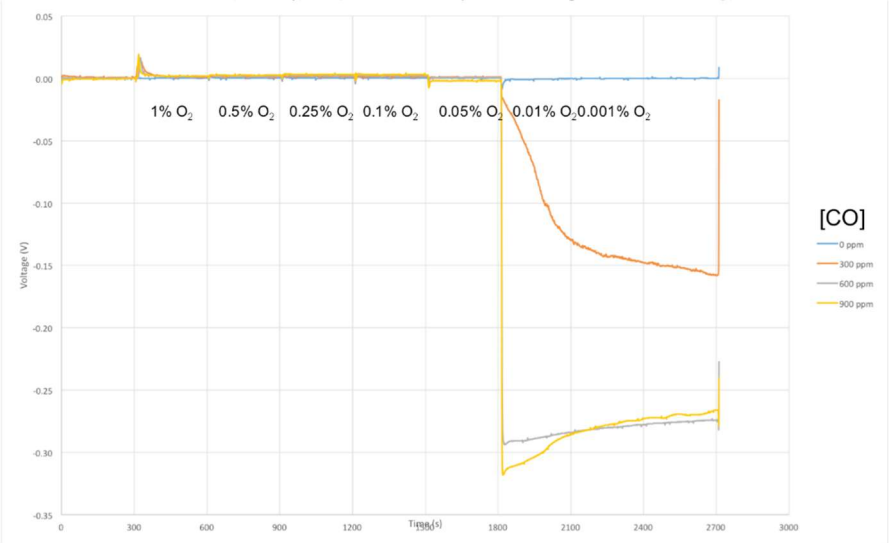

Figure 12. Response of a zirconia mixed potential electrochemical sensor using a La0.8Sr0.2CrO3 composition WE versus a dense Pt pseudo-reference electrode at 700°C versus PO2 for 0, 300, 600, and 900ppm of CO. The negligible voltage produced by this device in lean conditions shows that the electrodes generate identical voltages to the CO/O2 mixture at 700°C.

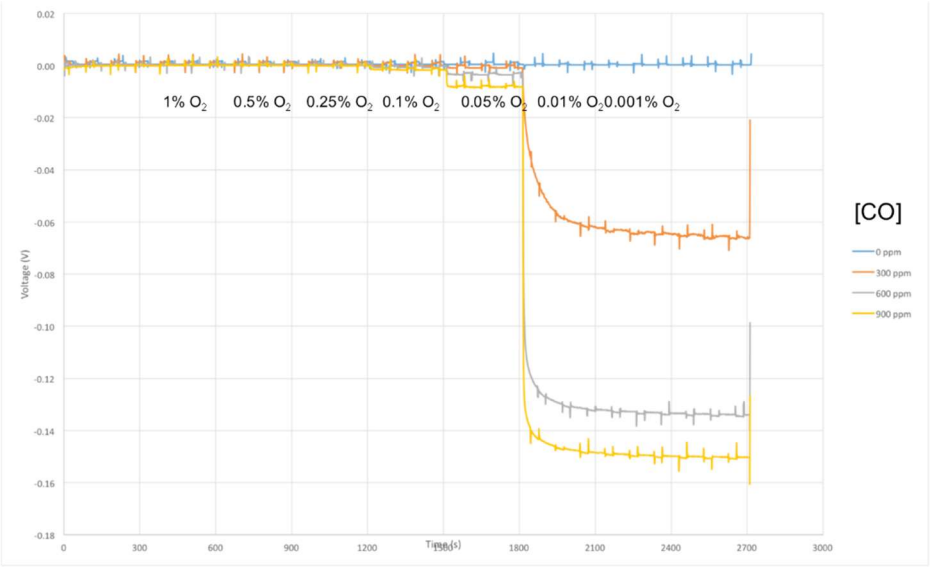

Figure 13. Response of a zirconia mixed potential electrochemical sensor using a La0.8Sr0.2CrO3 (80:20) composition WE versus a dense Pt pseudo-reference electrode at 900°C versus PO2 for 0, 300, 600, and 900ppm of CO. The negligible voltage produced by this device in lean conditions shows that the electrodes generate identical voltages to the CO/O2 mixture at 900°C.

At 700°C, and in lean O_2 conditions, a classic, non-equilibrium mixed potential electrode staircase response is obtained together with the expected trends with background PO_2 level are achieved with this device however, the voltage is low and 700°C is too low for application within a coal-

fired flue gas stream. The response of the device to up to 1750ppm CO of CO in 0.1, 0.5 and 1.0% O2 is shown in Figure 14.

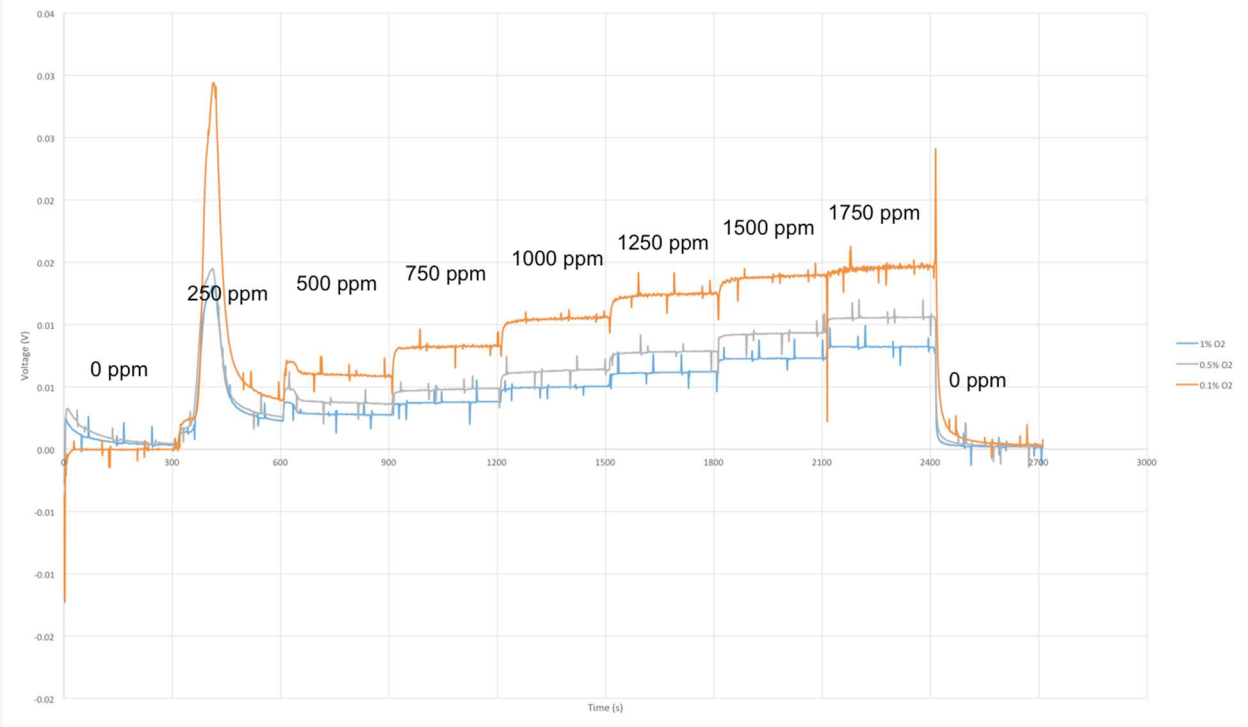

Figure 14. Response of a zirconia mixed potential electrochemical sensor using a La0.8Sr0.2CrO3 (80:20) composition WE versus a dense Pt pseudo-reference electrode at 700°C to CO and at 0.1, 0.5 and 1% PO2. Note the negligible voltage measured at 1%O2, which is considered the lower limit for lean combustion.

The level of Sr doping in LSCr perovskite has some impact on electocatalytic properties and a second pre-commercial device utilizing a La0.9Sr0.1CrO3 working electrode was tested under identical conditions. An identically prepared pre-commercial automotive stick sensor with the 90:10 WE composition was placed inside the same tube furnace for testing. Fig. 15 shows some improvement via sufficient difference in oxygen reduction and catalytic oxidation between he two electrodes to measure a voltage difference between different CO test gas compositions and background oxygen levels. Unfortunately at relevant PO2 levels, the voltage produced by the 90:10 WE is only slightly better than the 80:20 WE (inset Fig. 15).

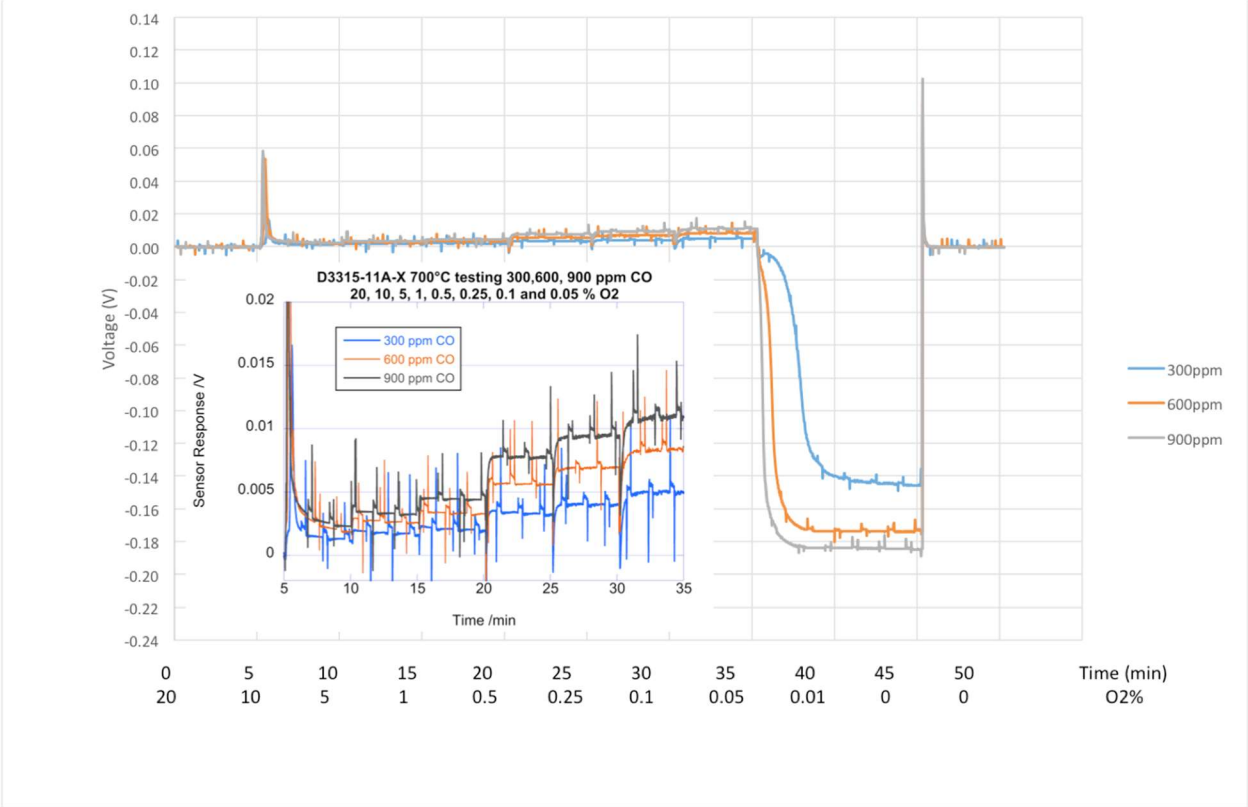

Figure 15. Response of a zirconia mixed potential electrochemical sensor using a La0.9Sr0.1CrO3 (90:10) composition WE versus a dense Pt pseudo-reference electrode at 700°C versus PO2 for 0, 300, 600, and 900ppm of CO. The negligible voltage produced by this device in lean conditions shows that the electrodes generate identical voltages to the CO/O2 mixture at 700°C.

The high level of noise in these data is an artifact of operating the stick sensor inside an electric tube furnace instead of heating with the sensor with the onboard Pt resistive heater as this noise is not normally present and must be a direct result of electrical noise from switching of the electric field of the furnace coils.

In order to study the effect of electrode surface area on sensor response and in particular, increasing the differences in rates of electro-catalysis and oxygen reduction, high surface area Pt ink was applied to the metal oxide and dense Pt metal working electrode and pseudo-reference electrodes respectively. Optimum ink firing conditions were first determined (Fig. 16 is an SEM image of a test electrode fired on 8mole% YSZ electrolyte) to yield morphology with much larger surface area than the completely dense, low-surface area electrodes engineered for the automotive stick sensors.

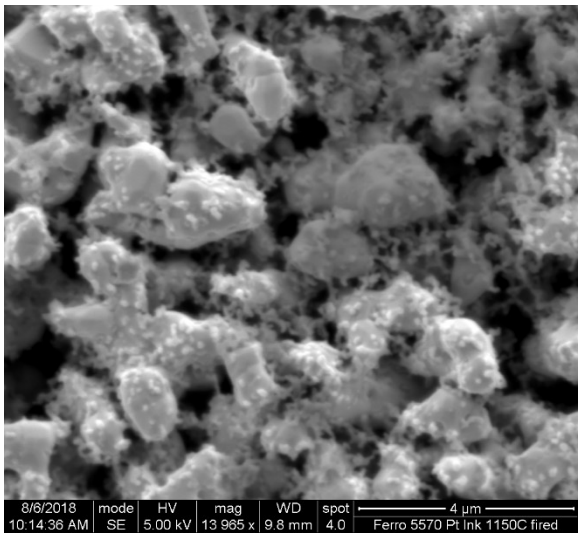

Figure 16. SEM image of a high surface area Pt ink (cat. no. 5570) acquired from ESL ElectroScience, final firing condition was 1100°C for 18h.

2. Pd-Au

Initial tests focused on two electrode measurements to evaluate differences in electrode kinetics at temperatures up to 900°C. Fig. 17 is the initial voltage response at 800°C for a background gas mixture of 2.5%O_2/5% CO_2/50% RH and only a negligible differential voltage was observed. At 900°C, the differential voltage was essentially zero. This result indicated that identical electrode potentials were being generated when exposed to CO.

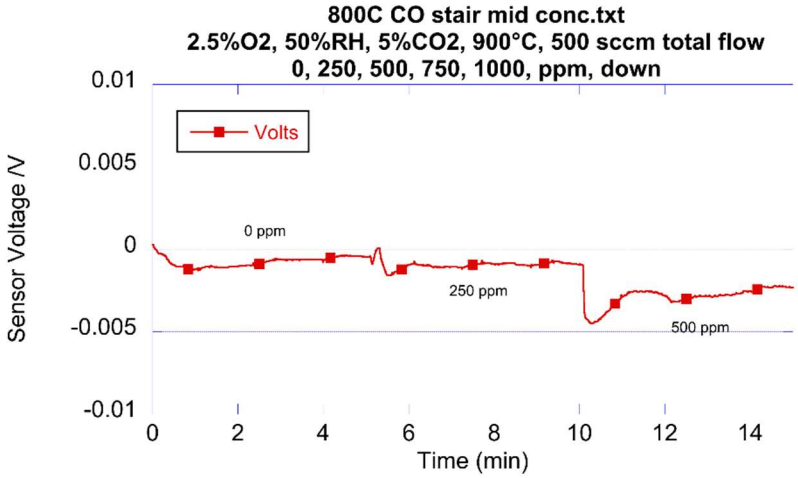

Figure 17. Sensor response of a Pd-Au/Pt//YSZ//Pt electrochemical button cell upon exposure to 250 and 500ppm CO in a background of 2.5%O_2/5% CO_2/50% RH. The voltage is measure between WE and CE.

The sample was annealed for 3 days at 900°C resulting in a break-in phenomenon often reported in the literature for classic, low T mixed potential electrochemical sensors fabricated with dense electrolyte-supported porous metal electrodes.

Fig. 18 is a plot of sensor response versus CO concentration up to 1500ppm in a 2.5%O_2/5% CO_2/50% RH gas mixture. A staircase response was observed up to 1000ppm CO and a large negative voltage was measure as stochiometry point was approached. Fig. 19 is a plot of sensor response up 1000ppm CO is the same base gas. The data show a staircase with slightly reduced voltage indicating some aging may have occurred after the 3-day anneal time. Fig. 19 shows that the electrode combination produced an appreciate differential voltage despite the high, 900°C temperature. At this point, the Pd-Au alloy WE produced the highest, high-T CO response to date.

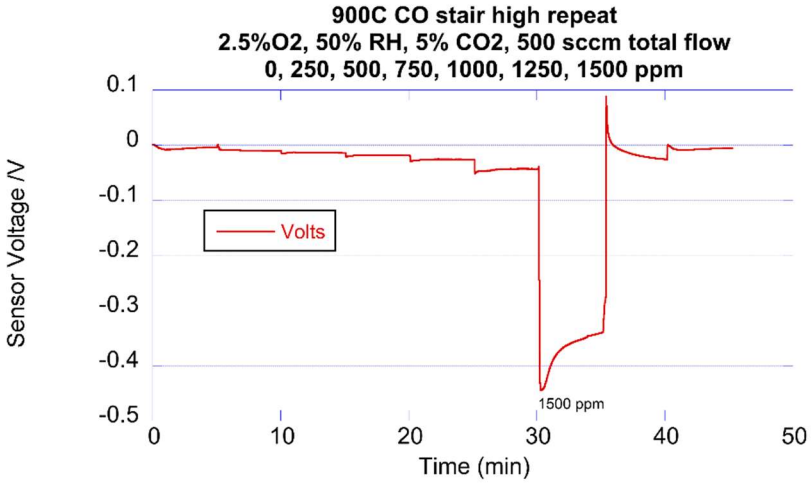

Figure 18. Sensor response of a Pd-Au/Pt//YSZ//Pt electrochemical button cell upon exposure to 250, 500, 750, 1000, 1250, and 1500 ppm CO in a background of 2.5%O_2/5% CO_2/50% RH after 3 day anneal at 900°C.

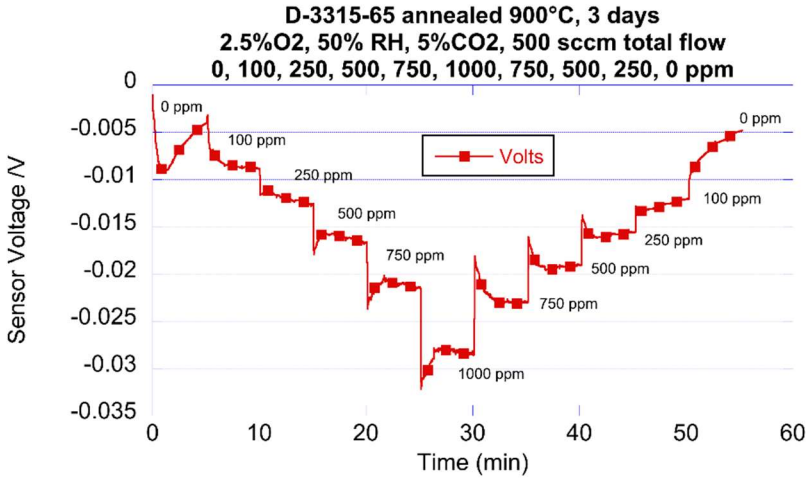

Figure 19. Sensor response of a Pd-Au/Pt//YSZ//Pt electrochemical button cell upon exposure to 100, 250, 500, 750, and 1000 ppm CO in a background of 2.5%O_2/5% CO_2/50% RH after 3 day anneal at 900°C.

PdAu-based sample in two-chamber testing with three voltage signals is also to be tested.Three signals can be monitored, which are the voltage differences between any two electrodes out of the total three electrodes: PdAu vs RefPt, FluePt vs. RefPt and PdAu vs. FluePt.
PdAu-RefPt = V_{PdAu} - $V_{RefPt;}$

FluePt-RefPt = V_{FluePt} - $V_{RefPt;}$

PdAu-FluePt = V_{PdAu} – $V_{FluePt.}$

The data is shown in Fig. 20-22. Similar with the data in the one-chamber test, PdAu sensor needs ageing to produce an observable response to ppm CO change. This phenomenon may be contributed to the morphological changes during the annealing, affecting the burning process of CO over the sensing electrodes surface.

However, the sensing performance between the one-chamber and two-chamber design is different. The sensing signal of PdAu-FluePt is smaller in the two-chamber test than in the one-chamber test. This may be ascribed to the difference in the flue gas composition. The two-chamber test focuses on the P_{O2} and CO concentration, while the one-chamber design was tested in a more simulated gas condition which contained CO_2, humidity, N_2, O_2 and CO.

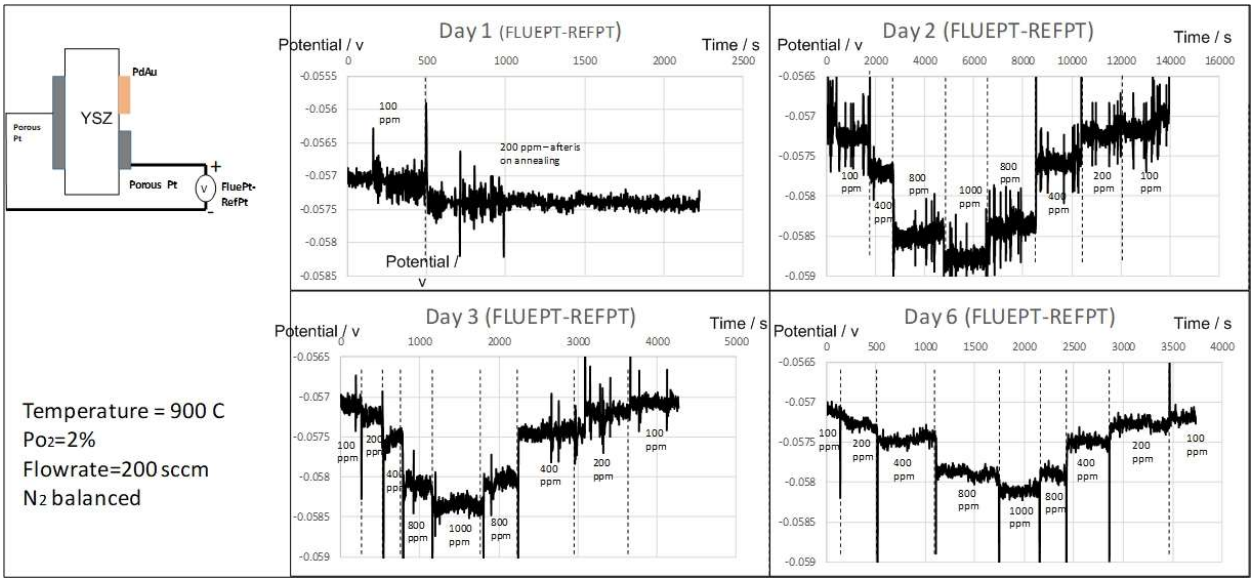

Figure. 20 The FluePt-RefPt signal of a PdAu-based sensor sample to the changing ppm CO in two-chamber design in a background of 2% O2 and balanced N2 at 900°C.

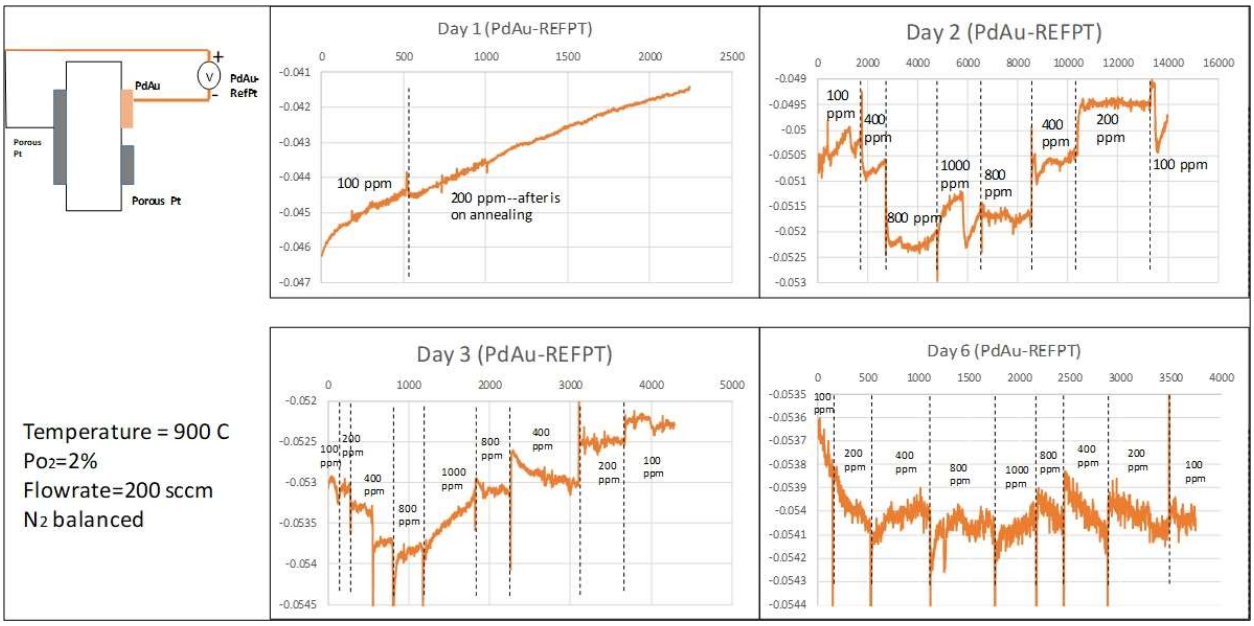

Figure. 21 The PdAu-RefPt signal of a PdAu-based sensor sample to the changing ppm CO in two-chamber design in a background of 2% O2 and balanced N2 at 900°C.

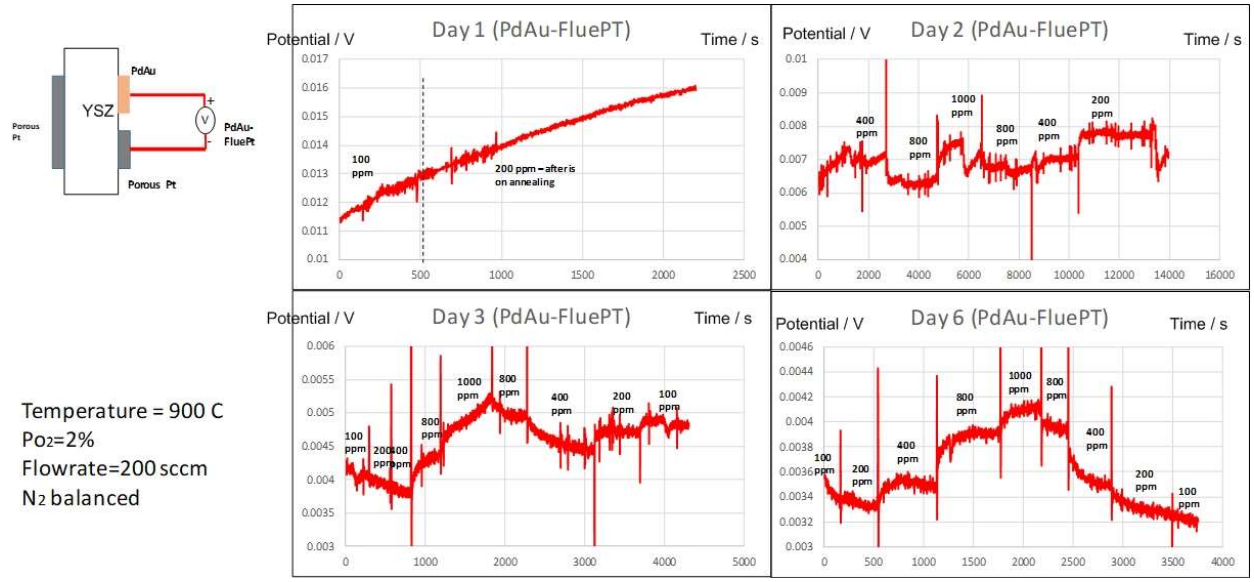

Figure. 22 The PdAu-RefPt signal of a PdAu-based sensor sample to the changing ppm CO in two-chamber design in a background of 2% O2 and balanced N2 at 900°C.

3. NiO

For the two-chamber configuration, the lab-scale sensor testing was conducted in 1000 ºC and a constant air flow was fed in the reference side. The flue gas consists of ppm-scale CO, air and N_2. During testing the CO concentration varied from 0 ppm to 1000 ppm in three oxygen concentrations that were 0.5%, 1.05% and 2.1%.

Three signals can be monitored, which are the voltage differences between any two electrodes out of the total three electrodes: PtRef vs. NiO, PtRef vs. PtFlue and PtFlue vs. NiO, as shown in Fig. 23(a).

$PtRef\text{-}NiO = V_{PrRef} - V_{NiO;}$

$PtRef\text{-}PtFlue = V_{PrRef} - V_{PrFlue;}$

$PtFlue\text{-}NiO = V_{PtFlue} - V_{NiO.}$

Fig. 23(b) shows the total sensing results (all three signals) in the P_{O2} = 2.1% and 1000 ºC, with CO concentration varying from 0 ppm to 1000 ppm.

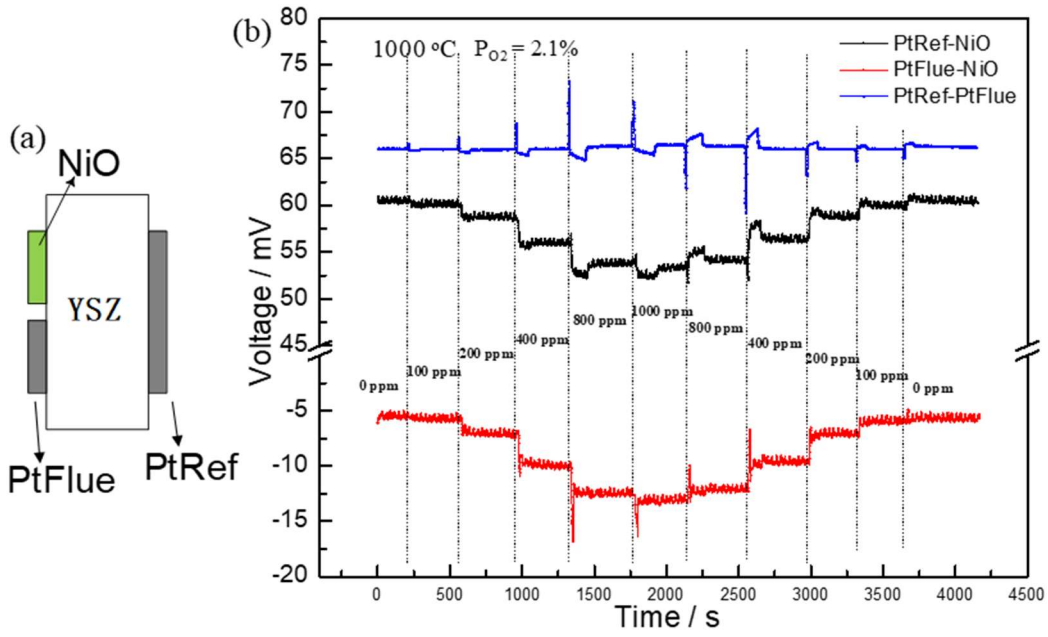

Figure. 23 (a) Schematic illustration of three electrodes in the sensor sample, and the voltage difference between each two electrodes was recorded. (b) The three signals variations with the changing CO concentration in the PO2 = 2.1% and 1000 oC. The flow rate of the simulated flue gas was fixed to 200 sccm; the flow rate of air is 100 sccm in the reference side.

Fig. 24 (a) and (b) are the enlarged data graphs in Fig. 23(b) of PtRef-PtFlue and PtFlue-NiO, respectively. The signal PtRef-PtFlue in Fig. 24(a) indicates the oxygen partial pressure change in real time in the flue gas side with the changing CO concentration. This can be supported by the evidence that when the CO concentration increases from 0 ppm to 1000 ppm, the signal increases around 0.6 mV. This value is coincident with the Nernst potential value of a 500 ppm oxygen concentration difference in this case, which is 0.65 mV. This phenomenon also indicates that Pt electrode is not very sensitive to the ppm CO concentration variation, but a good reference electrode.

In contrast to Pt electrode, the pure and dense NiO electrode exhibits a promising sensitivity to the ppm-scale CO change. The signal PtFlue-NiO shown in Fig. 24(b) exhibits a fast, clear, stable and repeatable response to the CO change from 0 to 1000 ppm. The sensing time is within 100 s, when

changing the atmosphere. Although the signal of 100 ppm CO only shows a slight distinction from 0 ppm, the signal starts to be much clear when the CO concentration reaches 200 ppm, especially in CO change from 200 to 400ppm and 400 to 800 ppm. The horizontal dash lines in Fig. 24(b) marks the values of signals and suggests the good reproducibility of the sensing results, because the signals for the same CO concentration are very close in the both forward and backward variations. Therefore, this sensor sample clearly demonstrates a good sensing ability towards <=800 ppm CO concentration in the P_{O2} = 2.1% at 1000 ^{o}C in the lab-scale power plant simulator. The sensing results in P_{O2} = 1.05% and P_{O2} = 0.5% are shown in Fig. 25 and Fig. 26, respectively. The sensor exhibits a good sensing ability as well in the atmospheres with lowered P_{O2}, when compared with P_{O2} = 2.1% which is a more aggressive environment for the sensor to detect the ppm CO concentration. Fast sensing time, clear signal distinction in different CO concentration, stable and reproducible signal values, are also achieved.

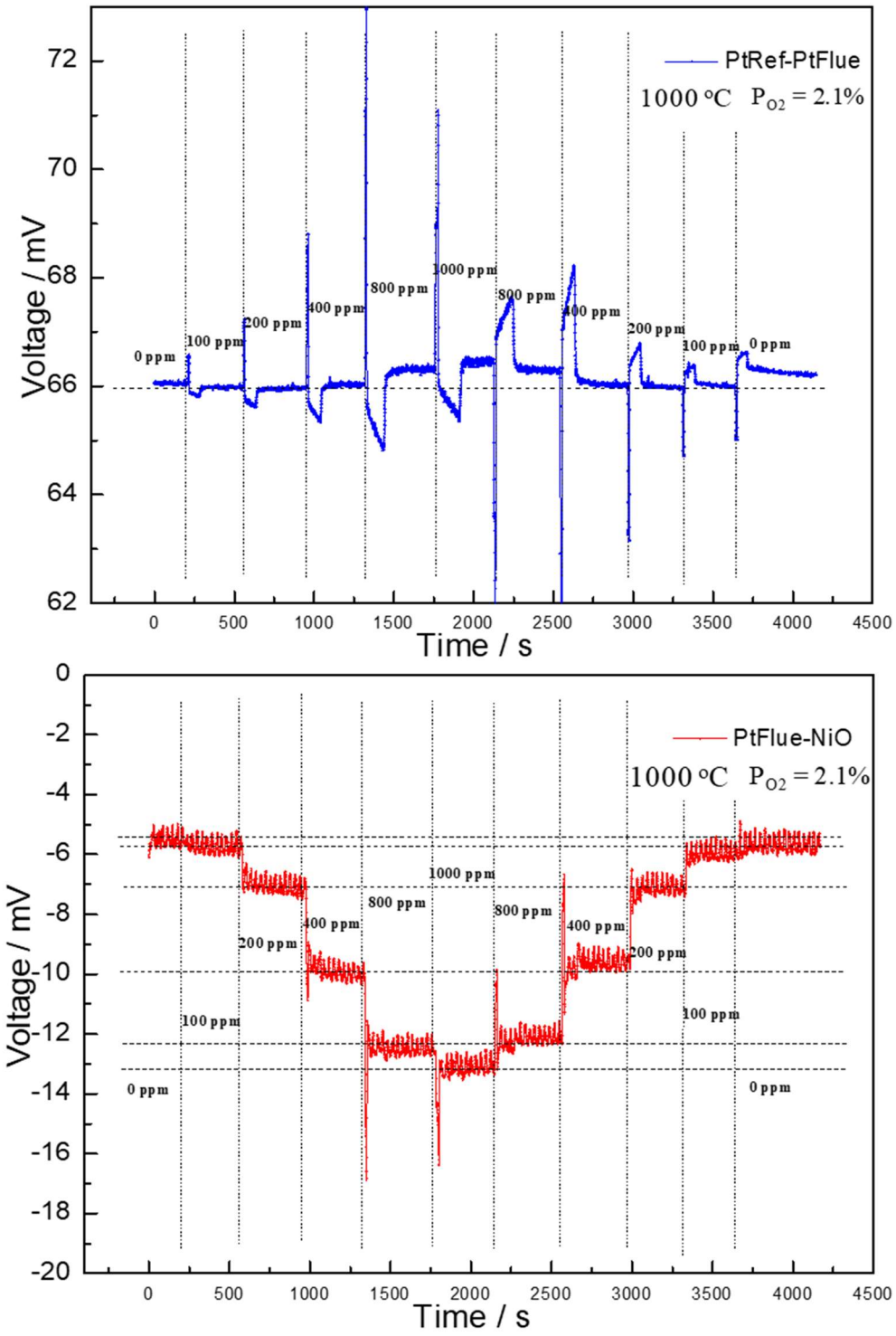

Figure. 24 Signals responding to the changing CO concentration in the PO2 = 2.1% and 1000 oC. (a) PtRef-PtFlue and (b) PtFlue-NiO. The simulative flue gas is composed of ppm CO, N2 and O2. The flow rate of the simulative flue gas is 200 sccm.

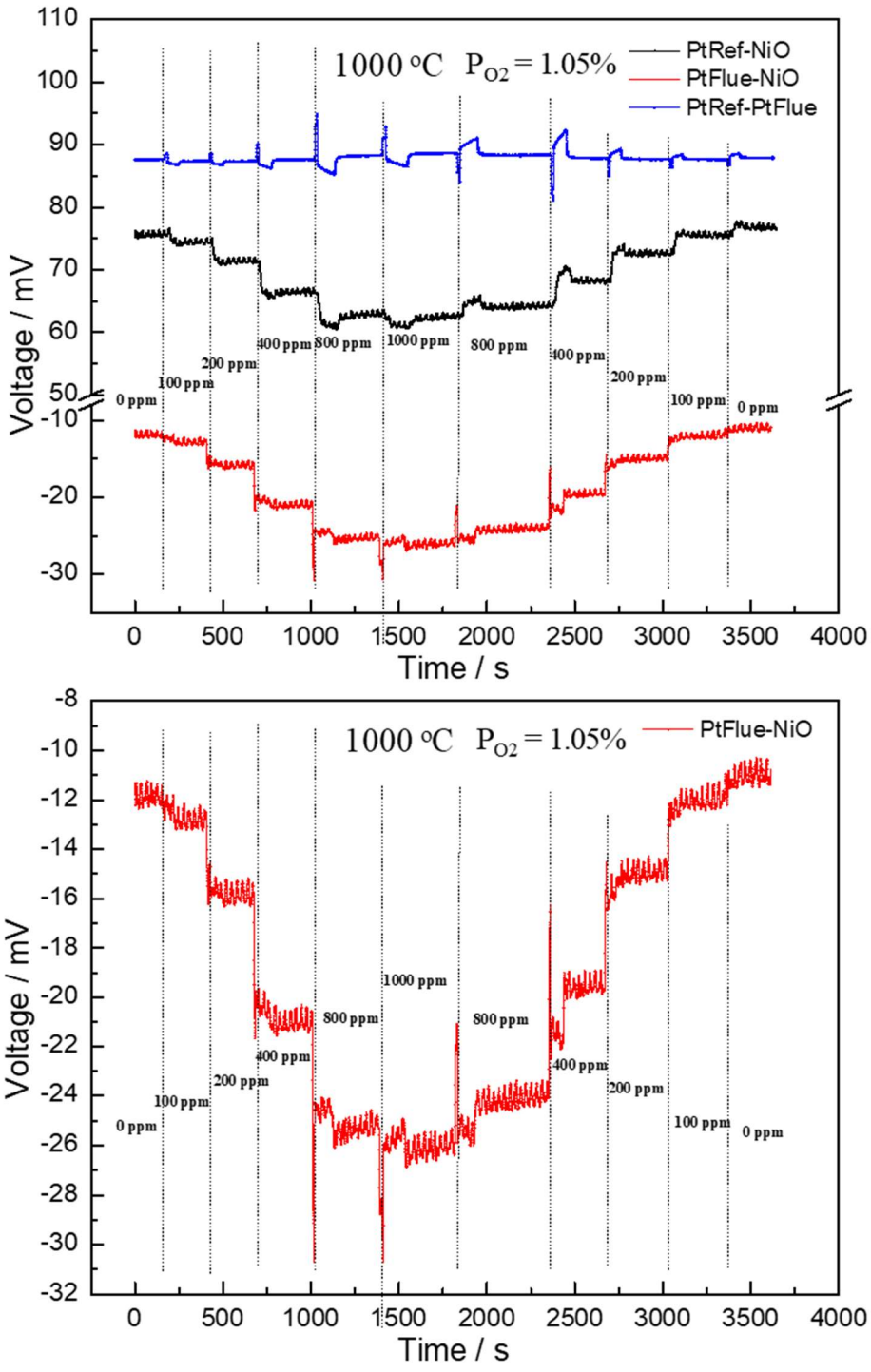

Figure. 25 (a) The three signals recorded in the PO2 = 1.05% and 1000 oC with the changing CO concentration from 0 ppm to 1000 ppm. (b) Magnified illustration of the signal PtFlue-NiO. The simulative flue gas is composed of ppm CO, N2 and O2.

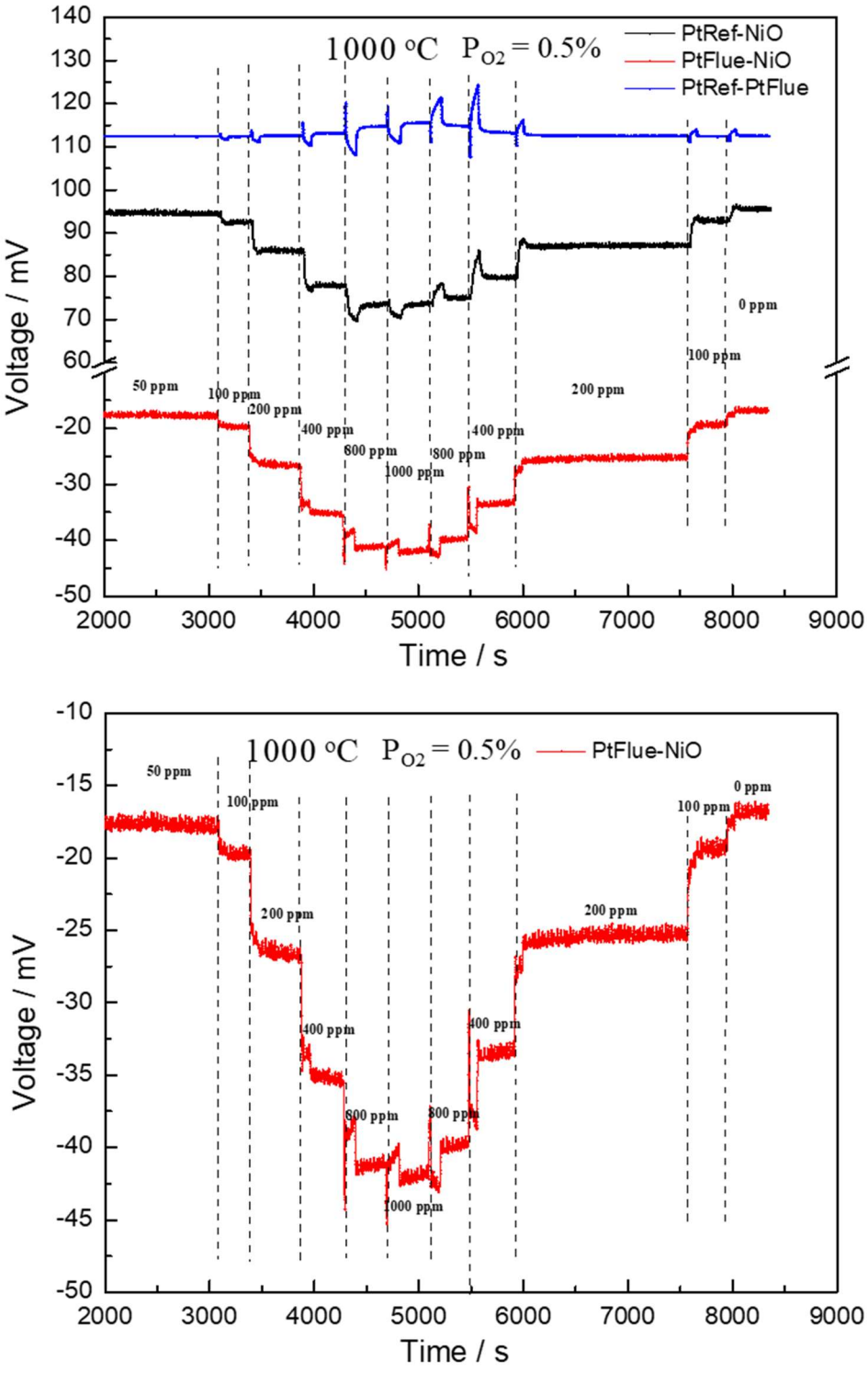

Figure. 26 (a) The three signals recorded in the PO2 = 0.5% and 1000 oC with the changing CO concentration from 0 ppm to 1000 ppm. (b) Magnified illustration of the signal PtFlue-NiO. The simulative flue gas is composed of ppm CO, N2 and O2.

The 3rd decision point requires that the sensing ability should be demonstrated towards <= 400 ppm CO concentration in a PO_2 range of 1-3% at 1000 °C in lab-scale power plant simulator.
Fig. 27 shows the sensing behavior of the developed sensor sample to the CO concentration ranging from 1000 ppm – 100 ppm – 1000 ppm under 1%, 2% and 3% PO_2 at 1000 °C. It is clearly demonstrated that the developed sensor design can achieve the signal of at least 13 mV in the oxygen partial pressure from 1% to 3%. Meanwhile, a good response time of around 100 s is obtained. The sensing stability is also good because in the cyclic change of CO concentration, the signal at every specific CO concentration is very close.

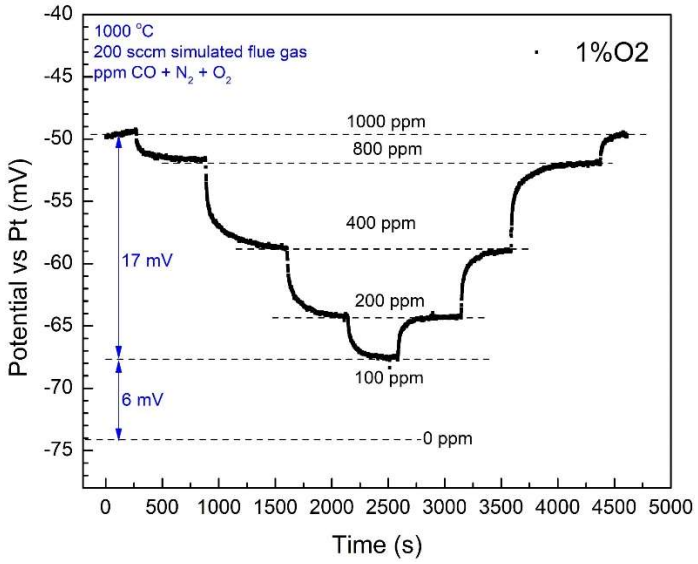

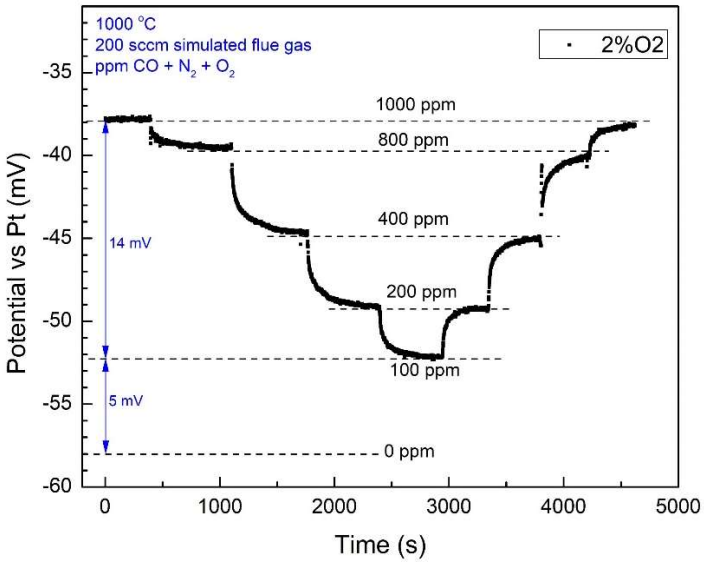

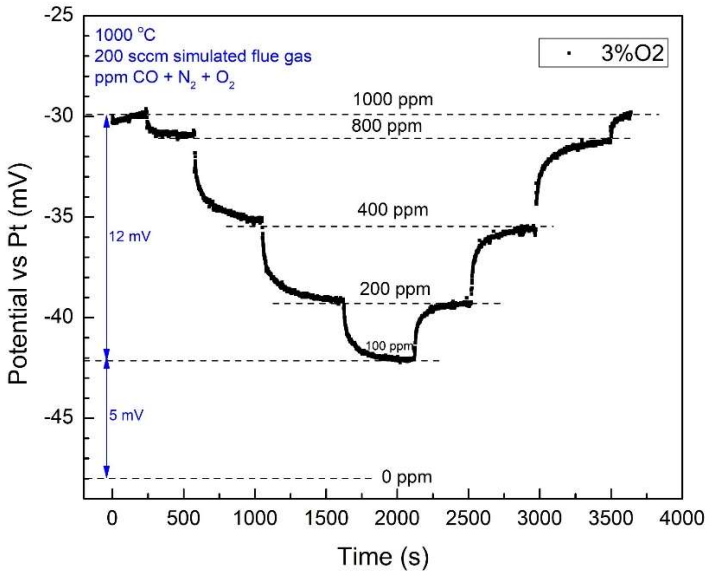

Figure 27 demonstration of the sensing behavior of the developed sensor sample to the CO concentration ranging from 1000 ppm – 100 ppm – 1000 ppm under 1% PO_2, 2% PO_2 and 3% PO_2 at 1000 ºC

To better understand the influence of morphology, the sensing signals of the porous NiO and dense NiO were monitored simultaneously. Fig. 28 demonstrates the sensing performance of the porous NiO to the ppm CO variation under 1%-3% O_2 and 900-1000 ºC. Although the performance is not stable when sensing in the 1% O_2, the porous NiO shows a repeatable behavior in 2% and 3% O_2 and the performance is even better in the higher temperature 1000 ºC than that in 900 ºC.

Fig. 29 shows the sensing behavior of the dense NiO electrode. It is worthy noting that the sensing behavior of the dense NiO electrode is much different from the porous NiO electrode. Firstly, the dense NiO doesn't show clear sensitivity to the ppm CO, especially in the high temperature 1000 ºC and the high oxygen concentration 2% and 3%. However, as shown in Fig. 10, porous NiO maintains the CO sensitivity which is around 9 mV for the 1000 ppm CO even in the most severe atmosphere that is 1000 ºC and 3% O_2. The second thing need to notice is the reversion phenomenon. For example, for the results in 3% O_2 and 900 ºC the signal decreases with the increase of the CO concentration. However, when the temperature is increased to 1000 ºC, the signal increases with the increase of CO concentration.

These phenomena proves that the morphology, at least the porosity, of NiO material can greatly influence the sensing behavior. A possible understanding is that the porosity of NiO is strongly related to the specific surface area and the total number of the active site of the NiO surface, further affecting the kinetics of the CO reaction with oxygen. Therefore, from the view of mixed-potential theory, the electrical potential of the electrode, governed by the kinetics of cathodic and anodic reactions over the electrode surface, is significantly associated with the porosity. This phenomenon also suggests the importance of getting more insights of the effect of morphology if we'd like to fabricate a reliable sensor.

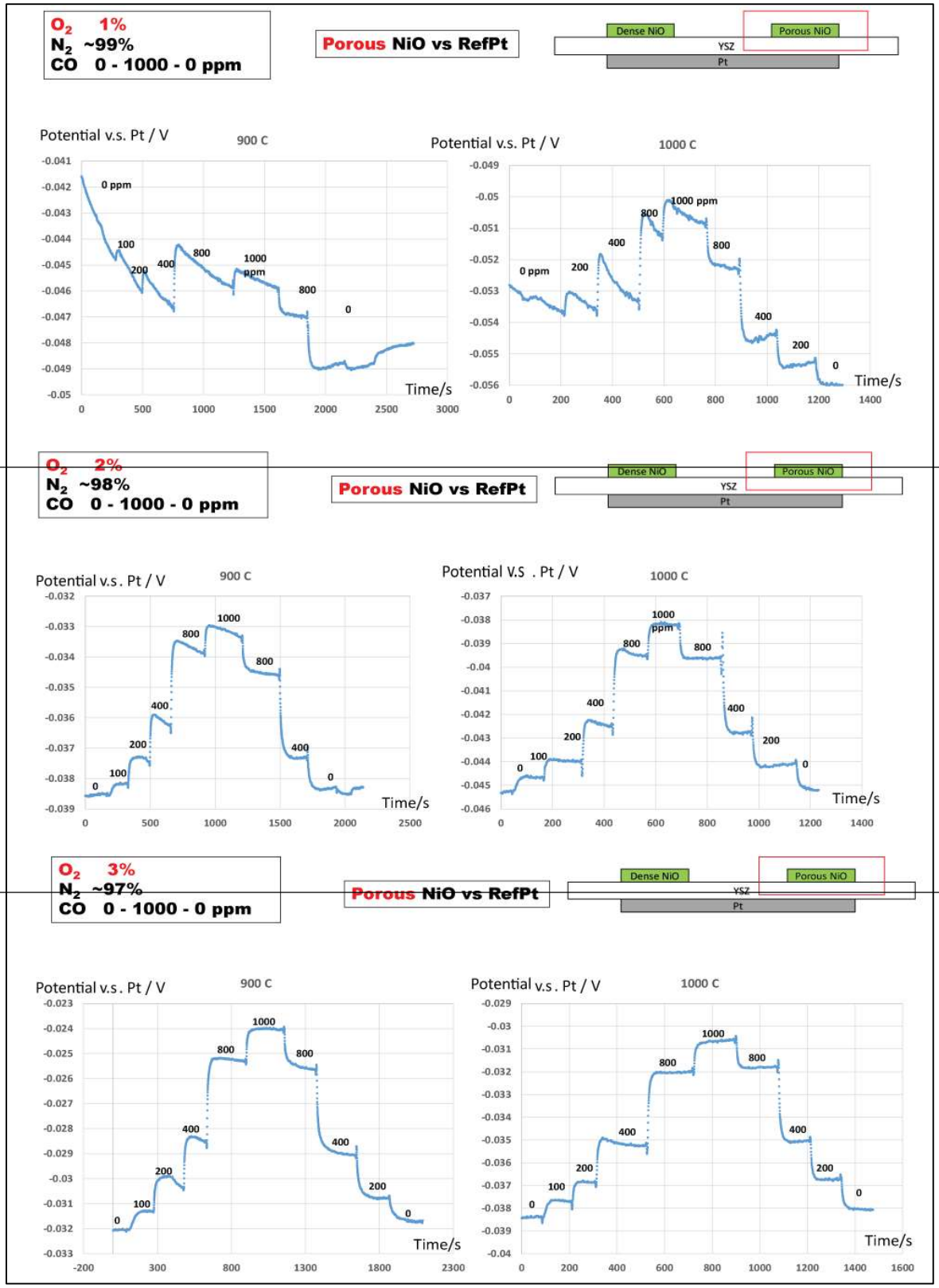

Figure 28 The sensing performance of the porous NiO to the ppm CO variation under 1%-3% O_2 and 900-1000 °C.

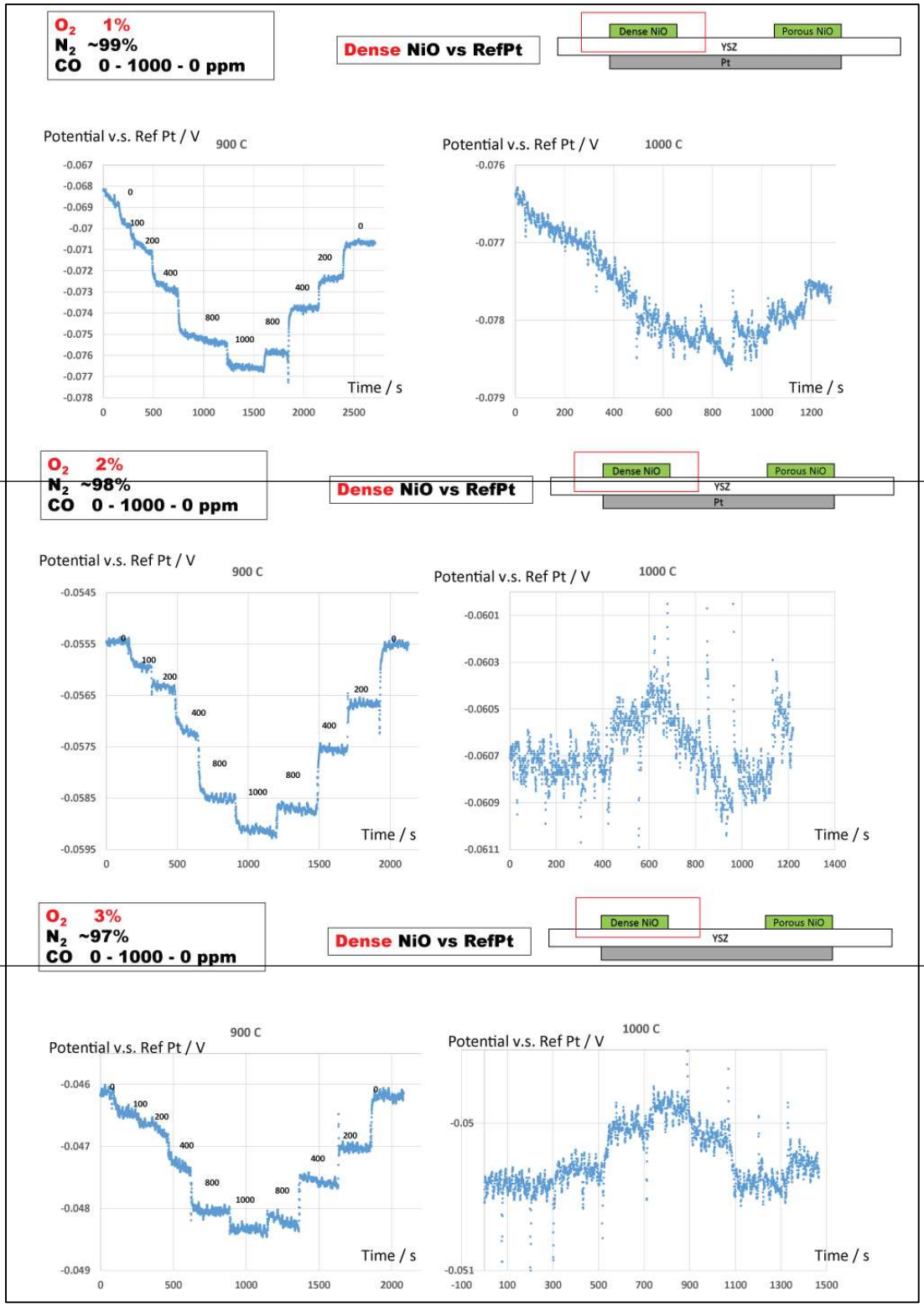

Figure. 29 the sensing performance of the dense NiO to the ppm CO variation under 1%-3% O_2 and 900-1000 ºC.

The selectivity of the sensor to other relevant gases, such as CO_2, steam and hydrocarbons, is important because these gases either are the major components in the real boiler atmosphere or

have great effect on the selectivity to CO gas. As a major component, CO_2 can account for 15% - 20% in the real boiler atmosphere of a coal-fired power plant. The effect of CO_2 on the sensing performance of CO is shown in Fig. 30. The red dash line is the point where the 10% CO_2 signal switches to 0% CO_2 Signal. It is shown that 10% CO_2 barely has effect on the signals, demonstrating a very low selectivity to CO_2 at a boiler level concentration.

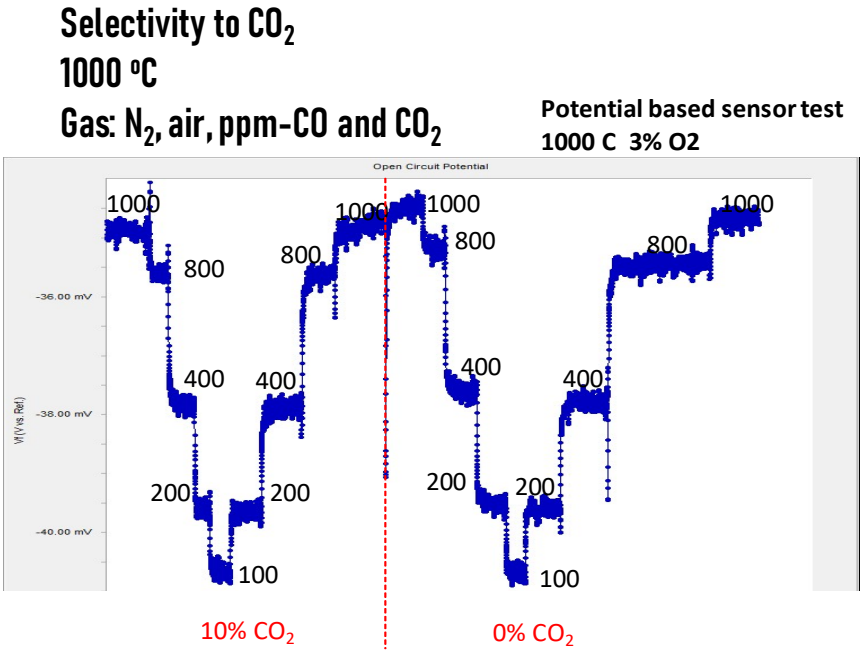

Figure. 30 The effect of CO2 on the sensing performance of CO

The effect of CH_4 on the sensing performance of CO is shown in Fig. 31. It is seen that the existence of CH_4 in the atmosphere only increases the fluctuation of the signal slightly. The median value keeps the same regardless of the presence of CH_4 at every CH_4 concentration level we have measured. It means the effect of CH_4 on the CO sensing is pretty low.

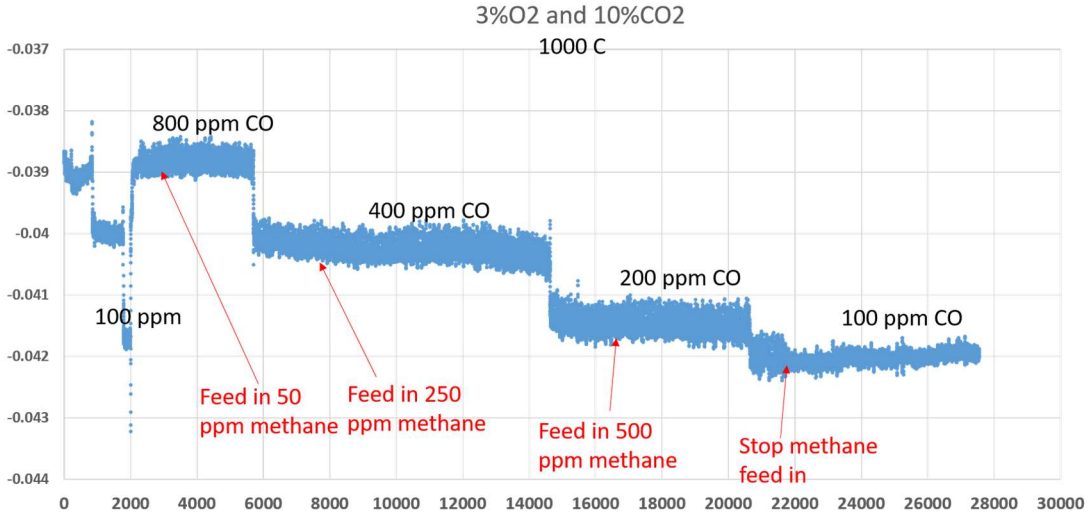

Figure 31 The effect of CH4 on the sensing performance of CO

The effect of H_2O on the sensing performance of CO is shown in Fig. 32. It is seen that steam can exert significant effect on the sensing of CO for the NiO-based sensor. It does not only decease the local oxygen partial pressure over the sensor surface, but also decreases the sensitivity of CO. In the next QTR, the effect of steam will be considered and investigated further.

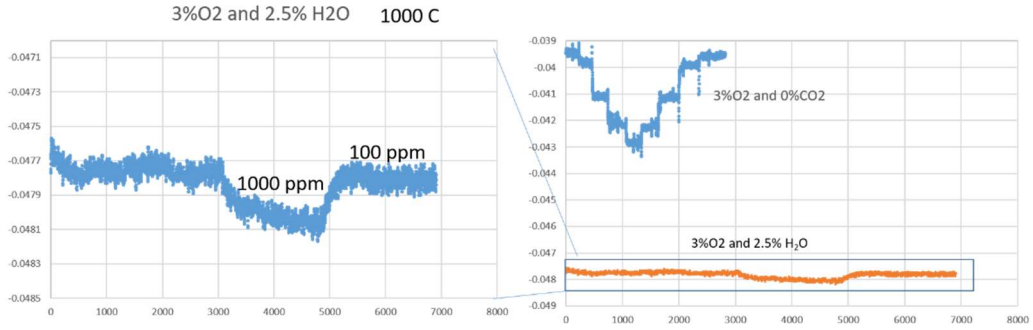

Figure. 32 The effect of steam on the sensing performance of CO

The effect of C_2H_6 on the sensing performance of CO is shown in Fig. 33. C_2H_6 greatly affects the sensing performance to CO. It is seen that the 50 ppm ethane makes the signal to fluctuate significantly, nearly moving off the selectivity to CO.

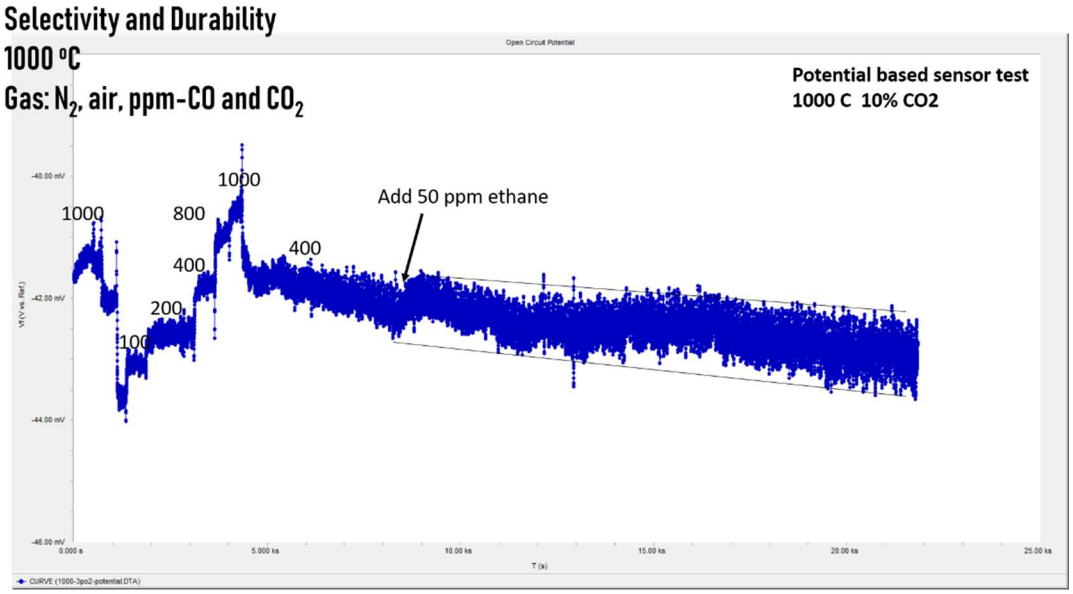

Figure. 33 The effect of ethane on the sensing performance of CO

One thing that should be examined is whether Pt electrode on the sensing side is only sensitive to O_2 rather than any other gases, because Pt electrodes in both sensing and air sides are used to measure the real oxygen partial pressure. The performance of Pt electrode in the sensing side is shown in Fig. 34 and Table. 1. It is shown that Pt is a good reference electrode, which is nearly only sensitive to O_2 concentration.

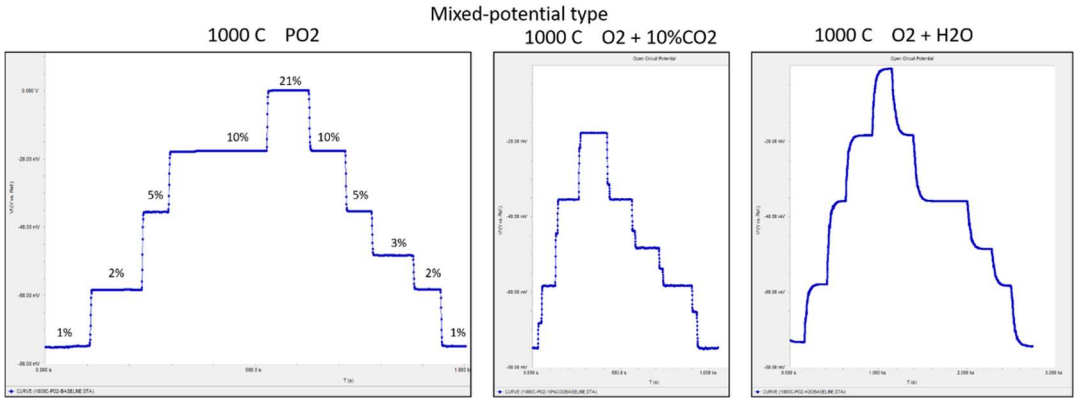

Figure. 34 Signals of Pt in sensing side corresponding to PO2 changes in CO2 and steam containing atmospheres

Table 1 Pt sensitivity to ppm-scale CO in different gas compositions

CO /ppm	3%PO2	3%PO2+20%CO2	3%PO2+H2O
100	-48.2	-48.4	-48.9
200	-48.2	-48.5	-48.9
400	-48.3	-48.5	-48.9
800	-48.4	-48.6	-49
1000	-48.5	-48.7	-49

Fig. 35 shows the lab-setup of how we study the effect of volumetric flowrate. With the inlet volumetric flowrate unchanged, we varied the distances between sensing electrode surface and the flue gas alumina tube. Position 1 is the nearest distance between the tube and electrode surface, with position 2 in the middle and position 3 the farthest. Therefore, position 1 should have a highest volumetric flowrate, while position 2 has medium flowrate and position 3 has the lowest volumetric velocity.

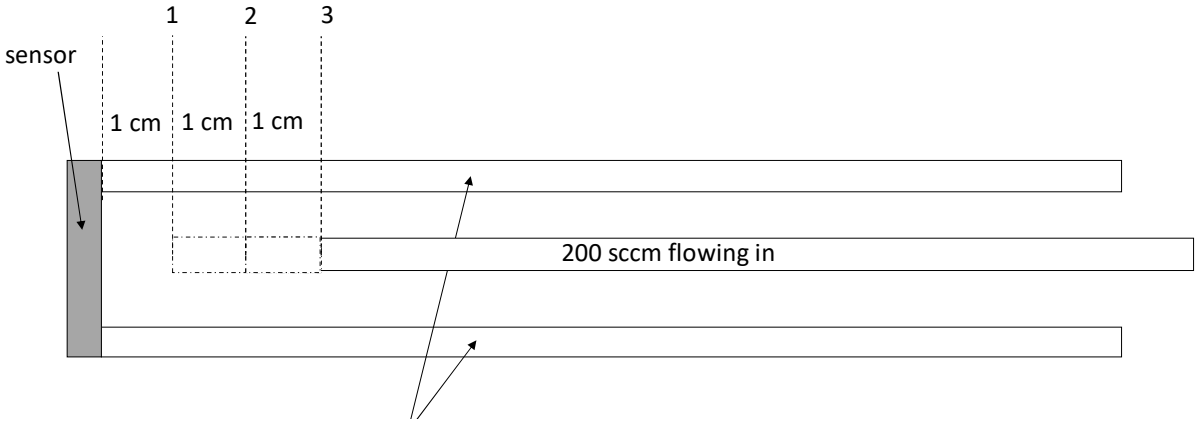

Figure. 35 The lab-setup of studying the effect of volumetric flowrate of simulated flue gas.

Fig. 36 shows the sensing signal baselines for varied oxygen concentration, excluding CO, while Fig. 37 demonstrates the sensing signals from varied CO concentrations. Both measurements were conducted at position 1, 2 and 3.

Fig. 36 depicts that the signal baselines are insensitive to the position of the gas conduct tube, meaning that the volumetric velocity of inlet gas doesn't affect the baselines. In contrast, Fig. 37 (a) illustrates the huge effect of volumetric flowrate on CO sensing. Position 1 has the highest sensitivity to CO partial pressure among the three positions. This result suggests that the CO diffusion in the porous NiO structure plays a key role in the sensing behavior of the NiO sensor. Fig. 37(b) further proves the results, where we didn't change the inlet simulated flue gas composition but moved the tube to different positions. It is shown that position 1 has the highest signal to the same 1000 ppm CO; at position 3, increasing the flowrate from 200 sccm to 300 sccm leads to the increase of the signal.

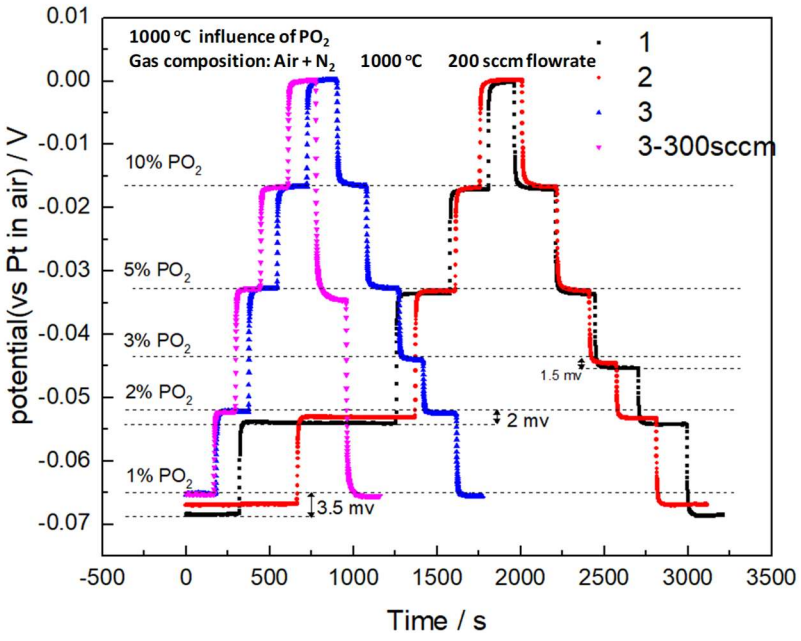

Figure. 36 The sensing baselines which only come from the oxygen concentrations because the gas only consists of air and N_2 excluding CO, conducted at position 1, 2 and 3

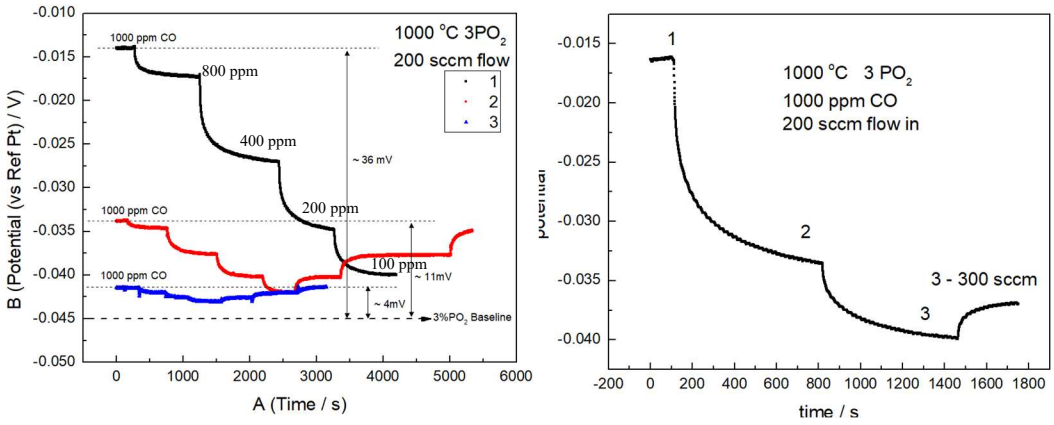

Figure. 37 (a) Sensing signals corresponding to the varied CO concentrations at 1000 ºC and 3% PO_2, (b) measurements were conducted at position 1, 2 and 3. Note, baseline signal is -0.045mV.

Fig. 38 illustrates three sensing samples with different porous NiO areas. The sensing behavior is demonstrated in Fig. 39. It is seen that large-area sample has the highest sensitivity. However, the medium-area sample doesn't show stab sensing ability to the CO gas. This may be due to a bad connection of electrode to the current lead wire .

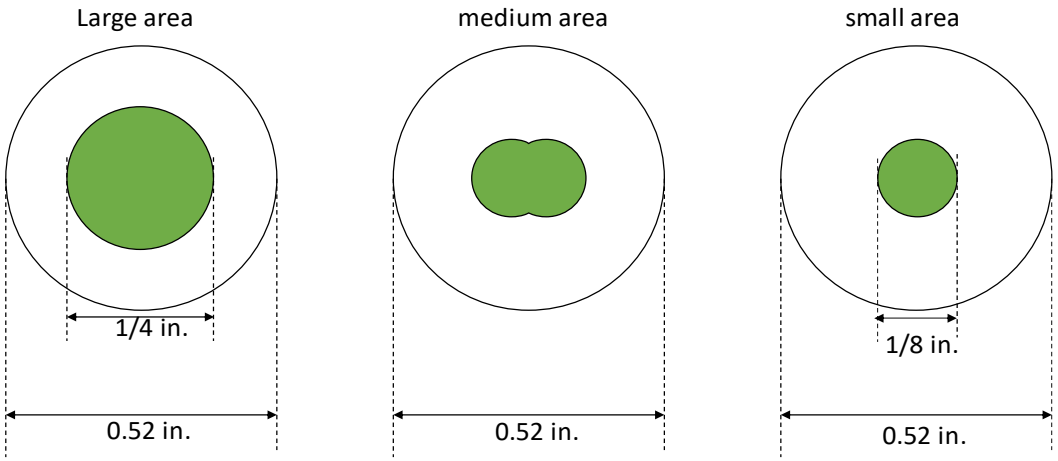

Figure. 38 Schematics of samples with different sensing electrode areas.

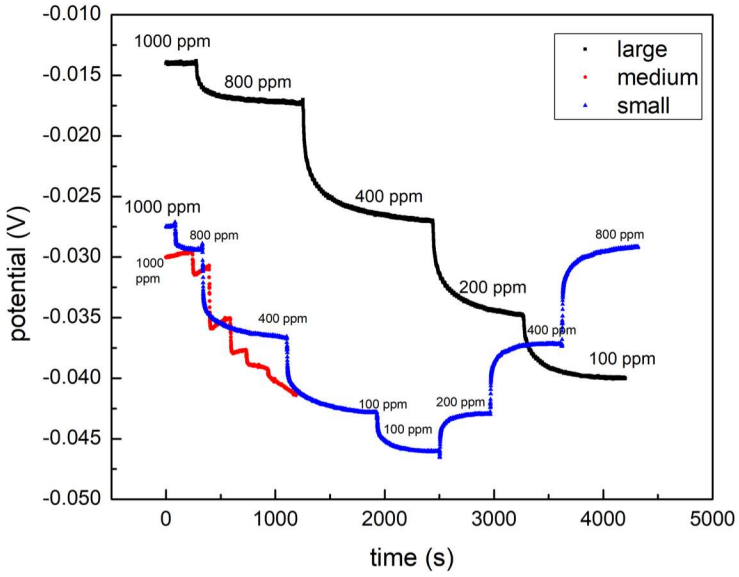

Figure. 39 The sensing signals of sensor samples with different sensing electrode areas, corresponding to the varied CO concentrations at 1000 ºC and 3% PO_2. Measurements were conducted at position 1.

Task 5.0 Post-Testing Characterization

SEM was used to characterize the morphology of the sensor sample after test. Fig. 40(a) and (b) show the SEM images of NiO interface ((b) is the magnified image). NiO electrode is proved to be dense. Fig. 40(c) and (d) show the Pt electrode cross section; Pt electrode is porous. NiO and Pt are assumed to be stable in the testing conditions, because these two materials are chemically stable in oxygen-containing atmosphere in 1000 ºC. The stability of these two materials can also be supported indirectly by the stable sensing performance during testing.

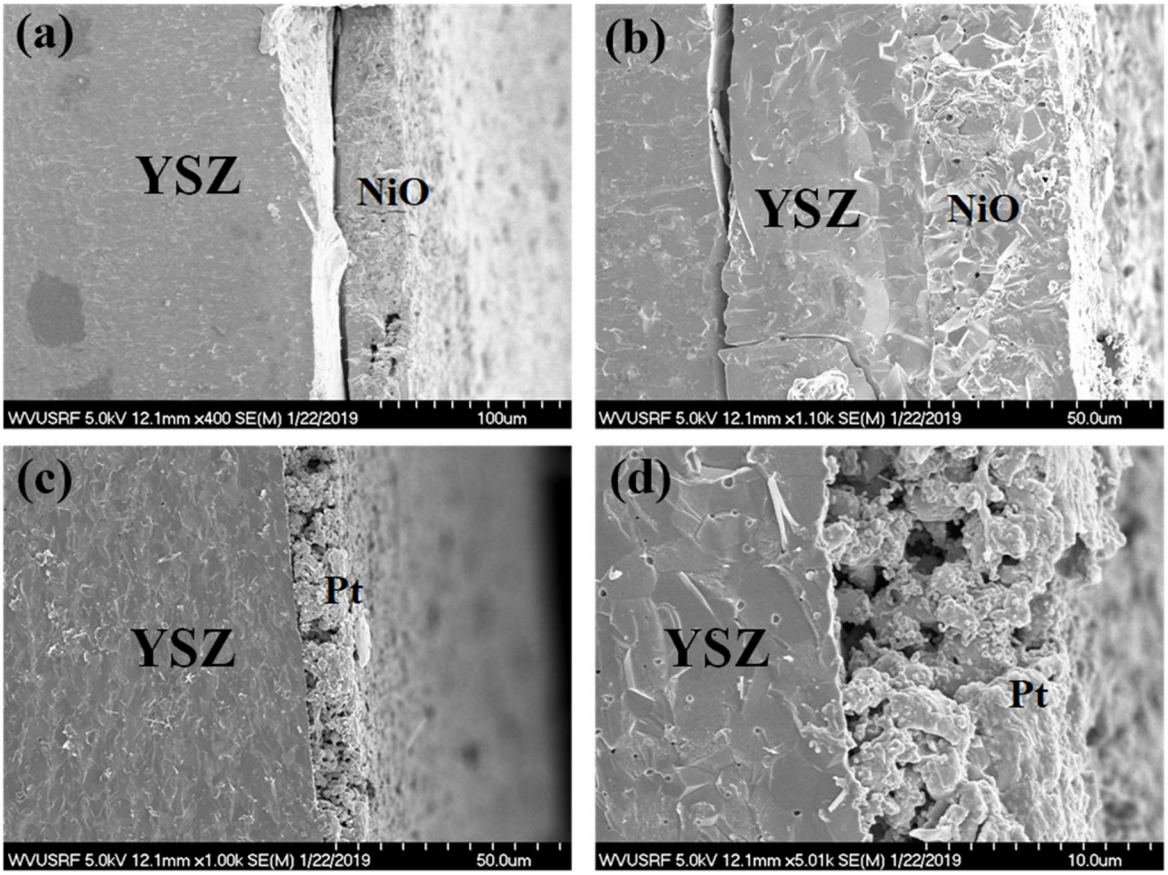

Figure. 40 SEM images of the cross section of (a)NiO electrode interface and (b) magnified image; cross section of (c) YSZ-Pt interface and (d) magnified image.

Fig. 41 (a) and (b) are SEM ESD and BSD images of the Pd-Au WE. The images show a completely dense morphology with no triple-phase boundary evident. The back-scatter detector (BSD) image shows that the surface of the WE is covered with small regions of low-Z residual sintering aids left over from the screen printing fabrication and firing of the electrode. Fig. 42 is a SEM BSD image of the edge of the WE. Here, there are small holes that increase the triple phase boundary area and presumably this is the dominant source of the increase in cell voltage observed during the initial 900°C anneal and break-in period.

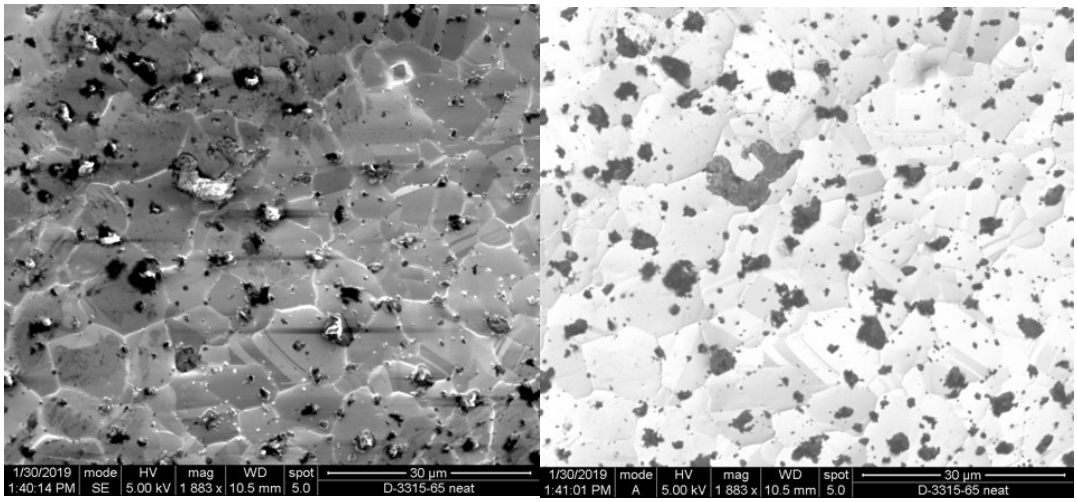

Figure 41 a (left) and 16b (right) of center region of the Pd-Au working electrode using ESD and BSD detectors respectively.

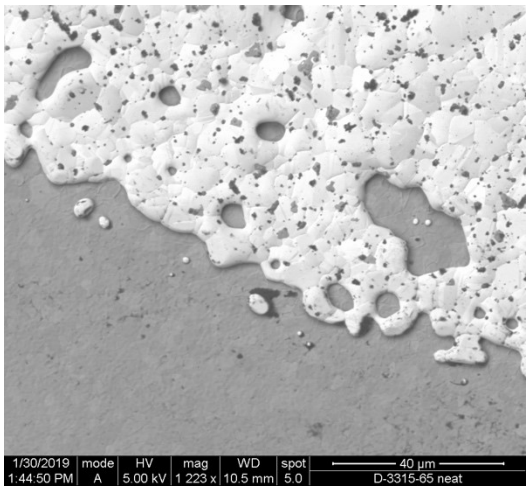

Figure 42. SEM BSD image of the Pd-Au working electrode.

Fig. 43 (a)-(b) show the as-prepared porous NiO structure before sensing testing using SEM. It is seen that the NiO particles are well-crystalized since facets and stairs can be clearly observed. Fig. 43 (c)-(f) show the SEM images of spent NiO after ppm CO in 1%, 2% and 3% O_2 testing and after annealing in 1000 ppm 2% O_2 for 1 h. It is seen from the (e) and (f), some tiny particles were grown on the NiO surfaces. Fig. 44 is the TEM images showing that the precipitated tiny particles may be certain amorphous phase. However, what material it is cannot be confirmed at this moment.

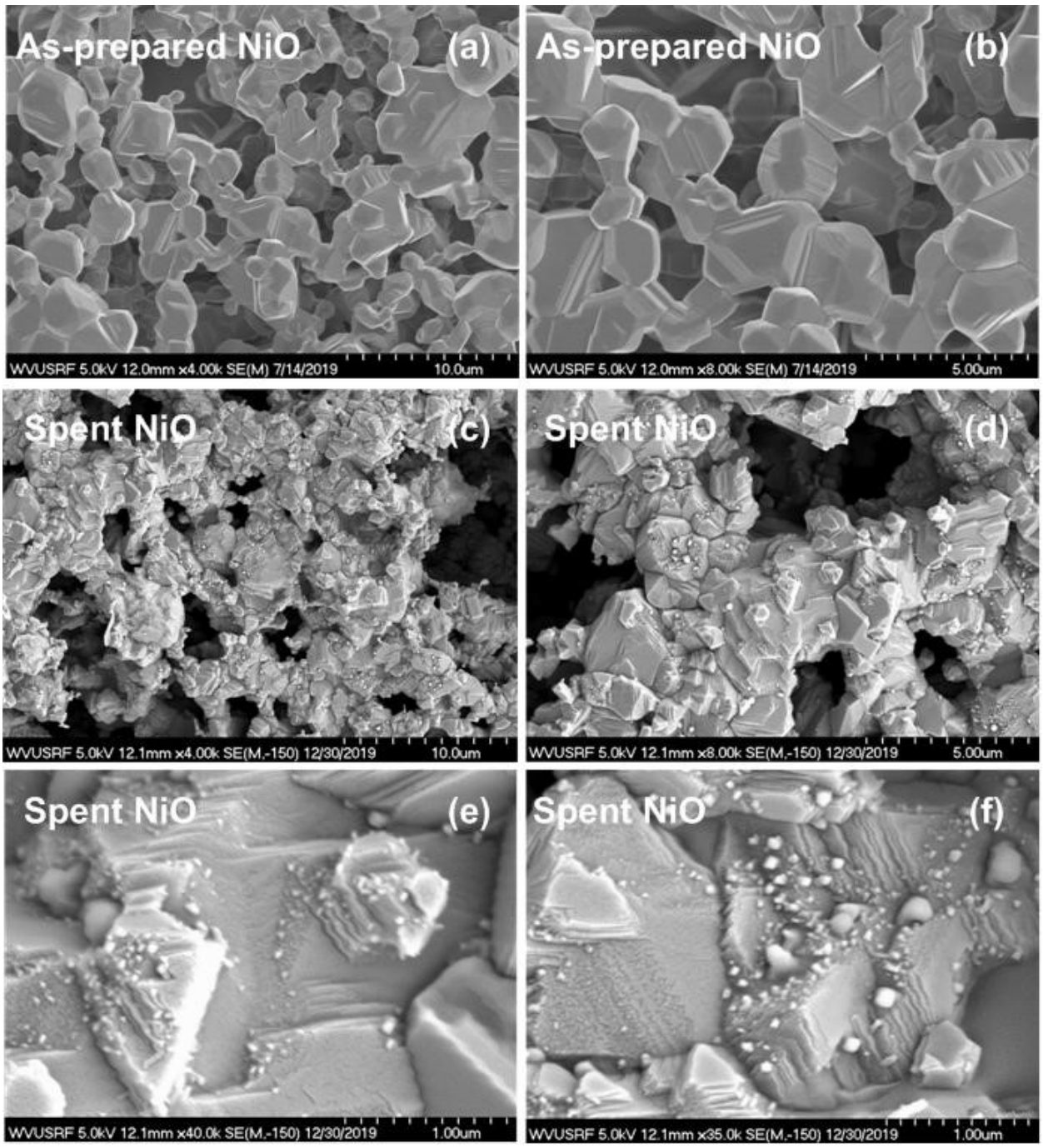

Figure. 43 (a)-(b) SEM images of as-prepared porous NiO structure before sensing testing. (c)-(f) spent NiO after ppm CO in 1% 2% 3% O2 testing and after annealing in 1000 ppm 2%O_2 at 1000 ^oC for 1 h, with different magnitude.

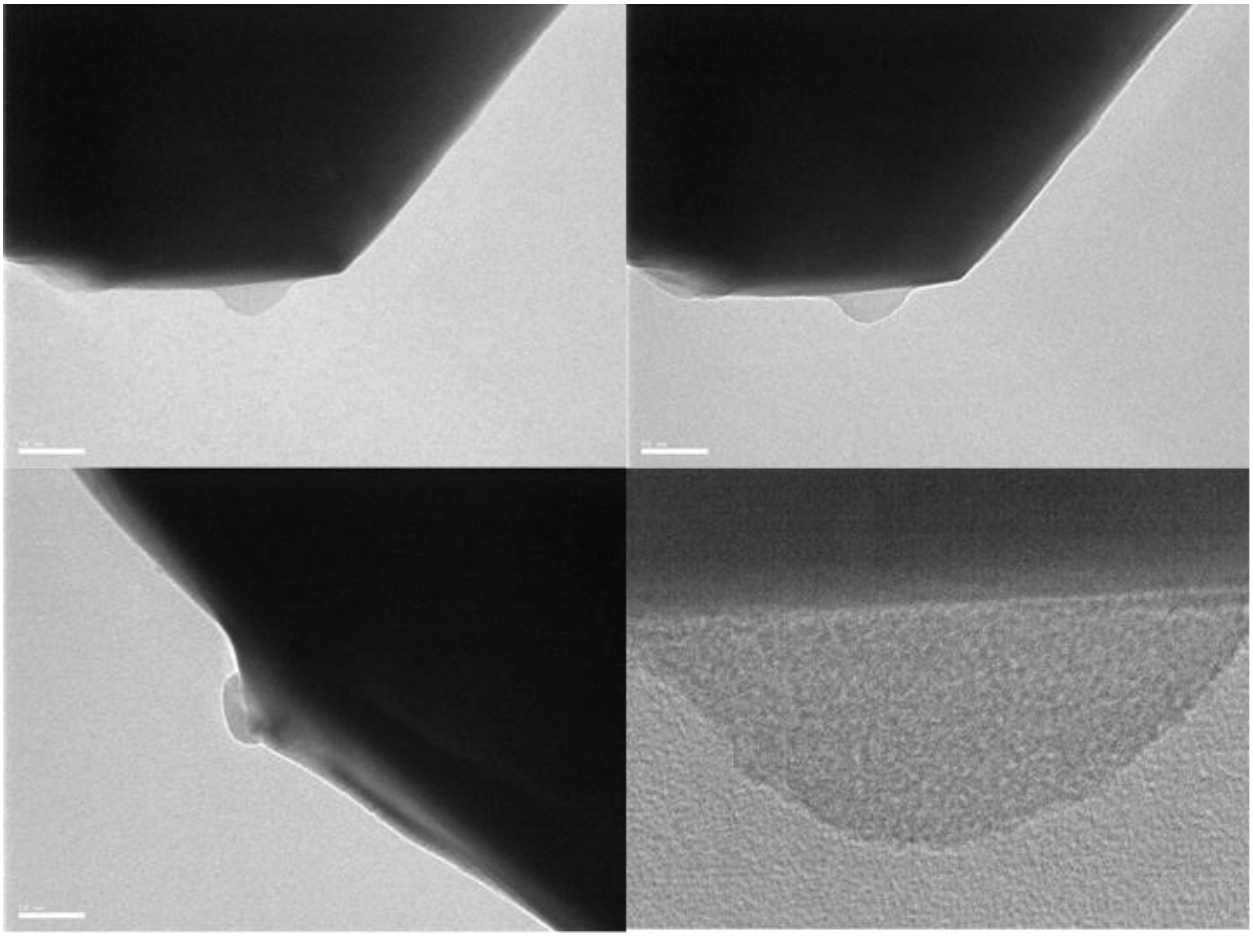

Figure. 44 Spent NiO after ppm CO in 1%, 2% and 3% O_2 testing and after annealing in 1000 ppm 2% O_2 at 1000 ºC for 1 h, with different magnitude.

Fig. 45 shows SEM images of different positions of the spent NiO over sensor surface after annealing for 24 h at 1000ºC and atmosphere of 1000 ppm CO and 2% O_2 balanced by N_2. The morphologies of different positions of the spent NiO surface are different, demonstrating the different stages of the CO-NiO interactions. In the center of NiO surface, needle-like phases grown or precipitated from NiO surface are very clear. Much fewer needle-like phases can be seen at the intermediate point of center and edge of NiO surface. NiO particles are full of holes at the edge, which may demonstrate what looks like the initial stage or nucleation process of the CO-NiO reaction.

Fig. 46 shows the magnified SEM images of the needle-like phases. It is seen that these phases are preferentially grown on steps or edges rather than on the facets. This is reasonable because steps and edges are places having more defects and thereby higher surface energy and catalytic reactivity. However, the fact that the facets are somehow invulnerable to CO may indicate that the CO-NiO reaction is not intense. This reinforces the significance of tuning the morphology of the sensor, in order to maximize sensor performance.

In the next quarter, more efforts will be put on characterization of the needle-like phases because it would be the key to understand the mechanism of how CO interacts with NiO. Xps, TEM and replica method would be employed to see the structure of the needle-like phases.

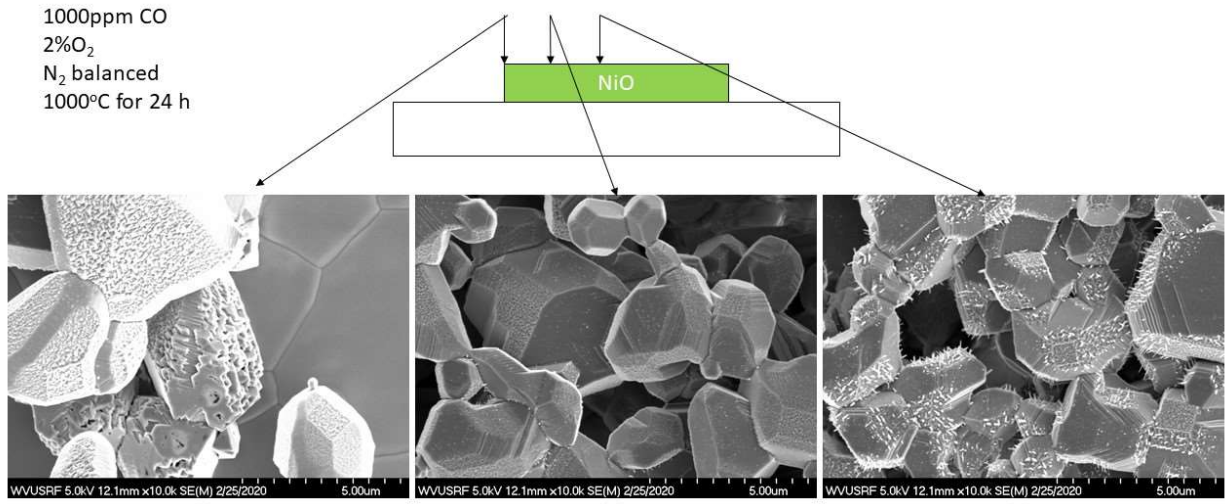

Figure. 45 SEM images of different positions over the spent NiO sensor surface after annealing for 24 h at 1000ºC and atmosphere of 1000 ppm CO and 2% O_2 balanced by N_2.

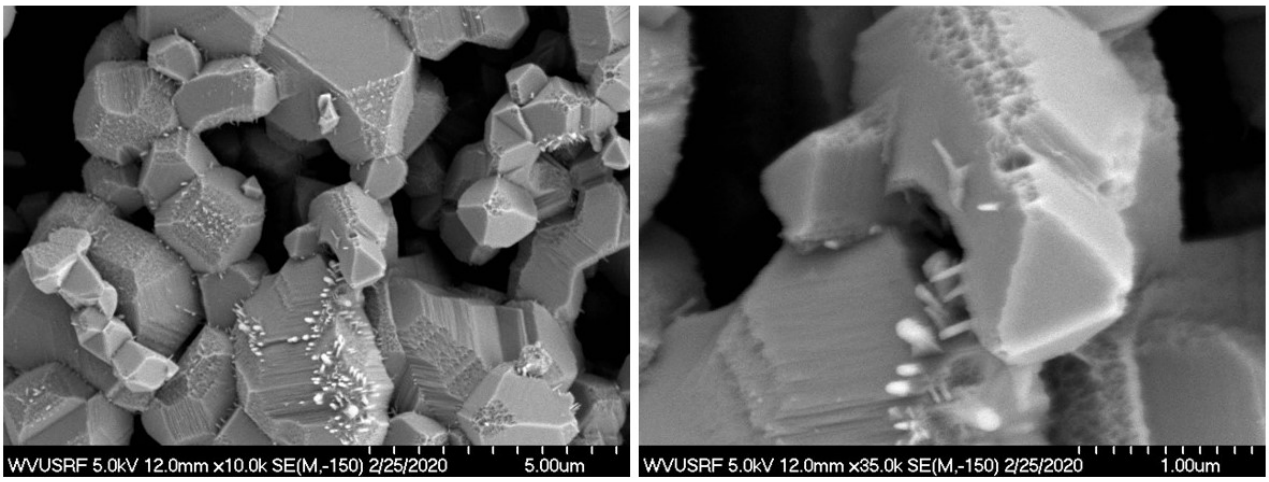

Figure 46 The magnified SEM images of the snitch-like phases.

Task 6.0 Electrochemical Mechanisms Investigation

The selectivity of the NiO-based mix-potential-type sensor to CO_2, CH_4, C_2H_6 and H_2O is examined:

1. Low sensitivity for **CO_2**, especially in low CO concentration regime
2. Low sensitivity for **CH_4**
3. Sensitive to **steam** which blurs the sensitivity to CO (but still show sensitivity to CO)
4. Very sensitive to **ethane** which nearly covers the CO signal.

To understand these phenomena, we would like to introduce one new conceptual understanding of what is electrical potential. The electrical potential can be defined as the "absolute" potential of an

electrode that equals to its work function in a practical atmosphere. It's worth noting that this work function is different from its usual meaning in physics which considers work function in a vacuum system. In electrochemistry, the work function in a real atmosphere means we consider not only the nature of a material but also the adsorbates over the material's surface. Therefore, if the adsorbates changes, the work function of the material would change, leading to the varying of measured potential.

Therefore, it can be considered that CO_2 is neither inclined to adsorb over the NiO surface nor to react with adsorbed oxygen because of the inertness of CO_2, which explains the low sensitivity of sensor to CO_2. In contrast, the higher polarity and activity of H_2O means that water molecule could easily interact with the NiO surface to modify its absorption status, either by replacing the adsorbed oxygen species over the surface or by reacting with the adsorbed CO to remove the CO. Similar thought can be applied to the high sensitivity of NiO sensor to ethane. The hydrocarbon can be easily oxidized by oxygen over NiO surface, leading to an obvious modification of the oxygen species coverage. As for CH_4, it is usually expected that sensing performance to CO in the CH_4-containing atmosphere should be similar with that of ethane-containing gases because both are hydrocarbons. However, the sensitivity to CH_4 is pretty low. One understanding could be that NiO surface is inert to CH_4 molecule and thus the presence of CH_4 could not modify the adsorption status of NiO, similar to CO_2. However, the weakness of this explanation is that CH_4 is in fact active over the NiO surface, which is also supported by many research results in catalytic methane decomposition. Therefore, it is more reasonable to believe that the low sensitivity of the sensor to CH_4 is due to the fully oxidization of methane before reaching the NiO surface, rather than to believe that CH_4 cannot modify the surface status of NiO.

The dependence of sensing behavior on the volumetric flowrate and sensing electrode area indicates the essential role of kinetics in determining the sensing signal. As illustrated in Fig. 47, porous structure of NiO hinders the CO diffusion into the TPB of NiO-YSZ interface. Thus, with the increase of flowrate, CO can reach the NiO-YSZ TPB with reduced hindrance, leading to a higher signal. Large area of sensing electrode showing higher sensitivity to CO is because more CO would be reacted at the TPB of NiO-YSZ interface since the larger reactive area results in higher retention time of CO reacting with active site over NiO surface.

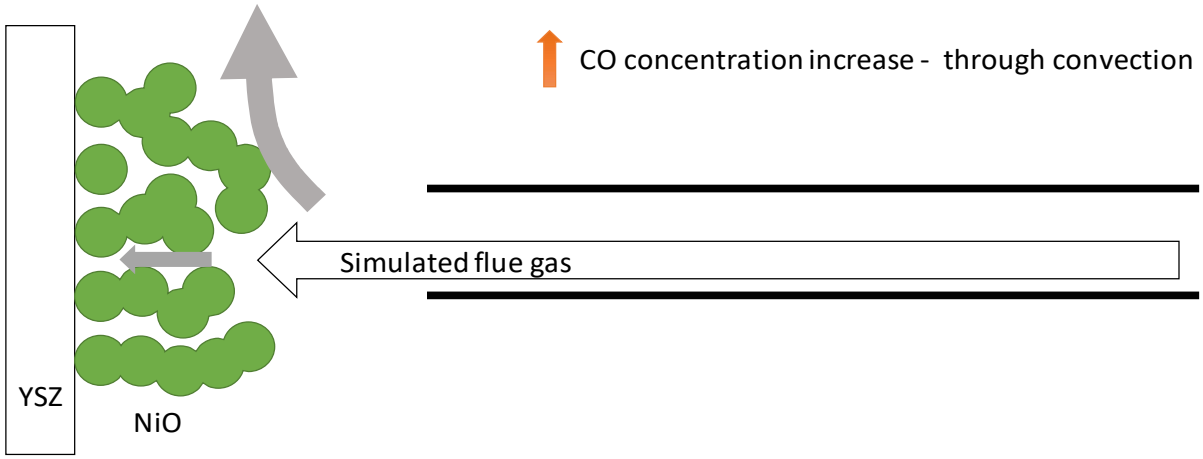

Figure. 47 Illustration of how sensing behavior is depending on the volumetric flowrate and sensing electrode area.

The positive relationship between sensor signal with the CO content found in this work is rarely observed in other works, which may indicate a new sensing mechanism. As studied in previous quarters, our evidence indicated that it may be the reduction of CO, rather than the oxidation of CO, that is primarily involved in the mixed potential formation. In this quarter, we have been engaged in finding more morphological and compositional evidence.

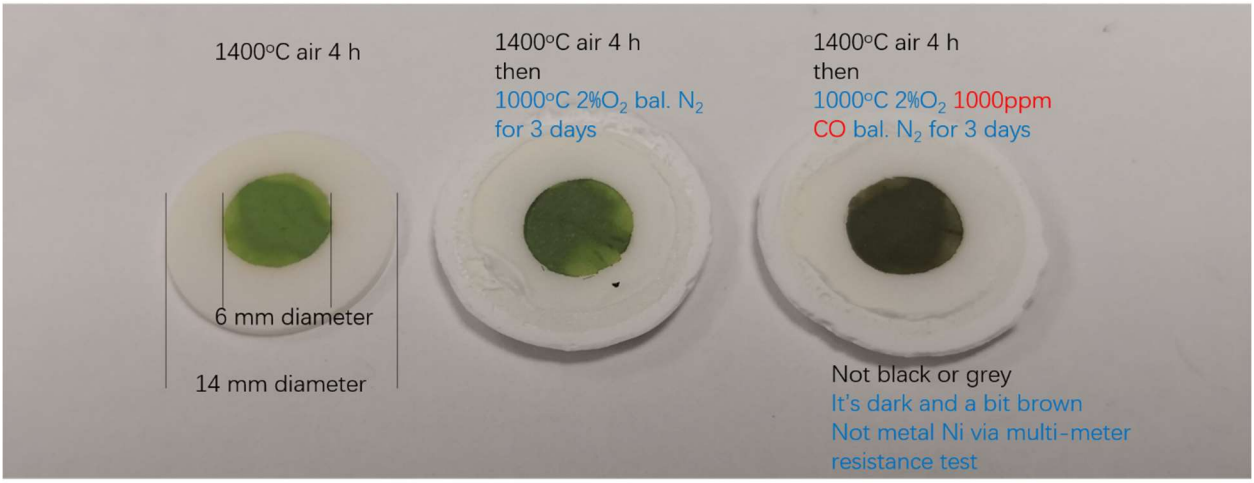

Figure. 48 Images of as-prepared sensor sample (left), after annealing at 1000 ºC 2%O_2 bal. N_2 without 1000 ppm CO for 3 days (medium) and at 1000 ºC 2%O_2 bal. N_2 with 1000 ppm CO for 3 days (right). During the cooling process, the samples were protected in the ultrahigh-purity nitrogen.

To magnify the morphology changes of NiO electrodes with and without CO in atmosphere, we annealed the as-prepared sensor samples (as seen in Fig. 48, sample in the left) for 3 days in the 1000 ºC 2%O_2 bal. N_2 with 1000 ppm CO (Fig. 48, sample in the right) and without 1000 ppm CO (Fig. 48, sample in the medium), respectively. Samples after annealing show clear color changes compared with the as-prepared sample, which is reasonable because NiO loses oxygen during the 2%O_2 annealing leading to higher oxygen non-stoichiometry and the darker color of the NiO electrode. It is seen that the sample with 1000 ppm CO annealing shows much darker or brown color than the one without 1000 ppm CO thermal treatment. This indicate influential role of CO.

Since we speculate the carbon deposition would occur on the NiO, the depth XPS were conducted to demonstrate the composition change. As shown in Fig. 49, carbon exists in NiO after 10 times 1-min sputtering for the sample annealed at 1000 ppm, while for the sample only annealed in 2% O_2, carbon is not detected after the 1st Ar^+ etching, the signal of which is due to the surface carbon contamination. Therefore, we have XPS results supporting the CO reduction reaction possibly occurred at 1000 ºC. Because of this mechanism is not fully in agreement with the normal sense, whether the CO reduction is occurred cannot be confirmed only by color change or XPS results. More sophisticated characterizations should be designed and conducted.

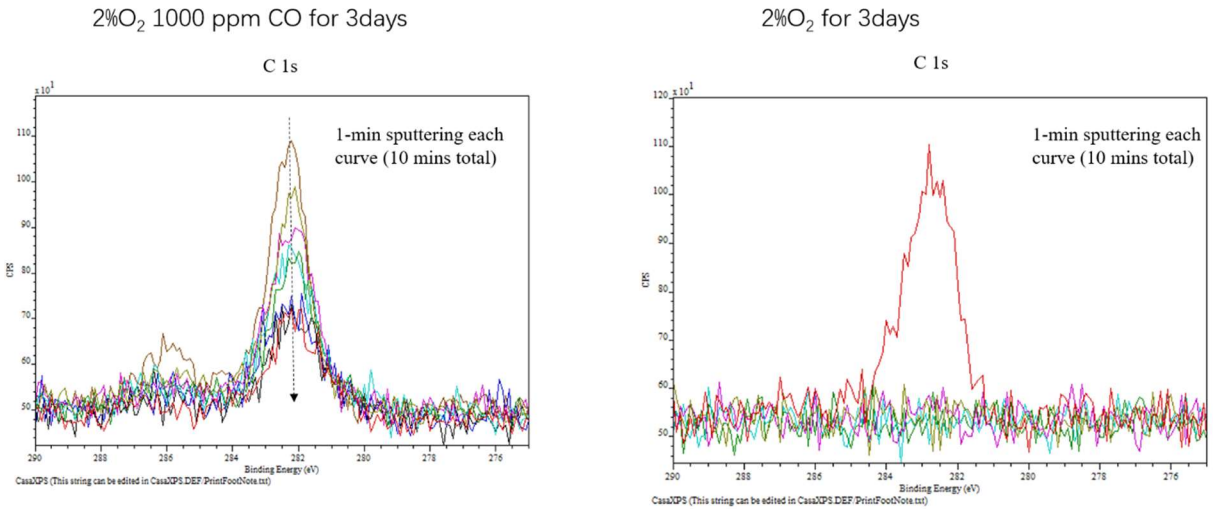

Figure. 49 Depth XPS results of the C 1s peak for the samples annealed at 1000 ^{o}C 2%O_2 bal. N_2 with 1000 ppm CO for 3 days (left) and at 1000 ^{o}C 2%O_2 bal. N_2 without 1000 ppm CO for 3 days (right)

Task 7.0 Sensor Testing in Utility Boiler

The design of sensor tested in the Longview Power utility boiler is illustrated in Fig. 50. In this design, the outermost layer is a stainless steel shield, which is used to prevent the water spray from contacting the inner alumina tube. Water spray is a standard periodically procedure to remove the oxides formed on the water-cooling wall. If the water contacts the alumina tube of our sensor design, the huge temperature gradient would crack or shatter the alumina tube. Between the outer stainless steel shield and the inner alumina tube is asbestos which is used to buffer the collision between the stainless steel shield and the alumina tube because in the utility boiler, the firing process results in violent shakes of the water-cooling wall. The combined application of the stainless steel shield and alumina tube is to make a safe chamber for the fragile sensor top, protect it from water spray and mechanical shaking. The sensor is all made of ceramic materials which is extremely vulnerable to thermal shock. Ni-Cr thermal couple was used to determine local temperature of our sensor.

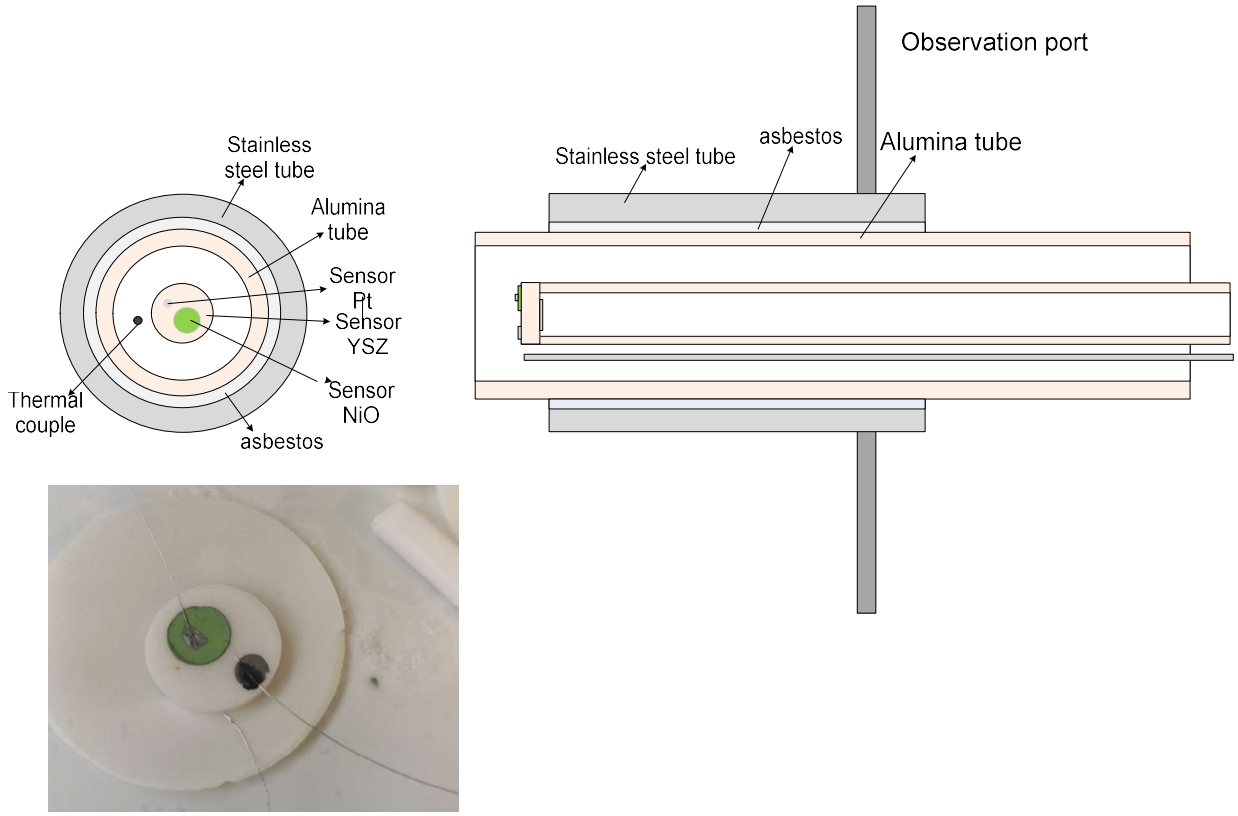

Figure. 50 Illustration of the sensor and package design for the utility boiler test in Longview Power.

Fig. 51 shows the sensing test result of the designed sensor assembled in Longview's utility boiler. The duration of the testing is approximately 20 hours. In the first hour, the connection between FluePt electrode and RefPt electrode was broken. After 20 h testing, the connection between NiO electrode and RefPt electrode was broken, resulting in the whole testing shutdown. The signal (potential difference between NiO and RefPt) from NiO electrode was shown in Fig. 51(a). An abrupt drop of signal can be observed after 1 h testing. We speculate that after 1 h test, the wire of NiO electrode was contacted with FluePt electrode, leading to the signal of NiO being overridden by the signal of FluePt electrode. Therefore, in this testing, we believe that only the first 1 h data could be viewed as valid and needs to be further analyzed.

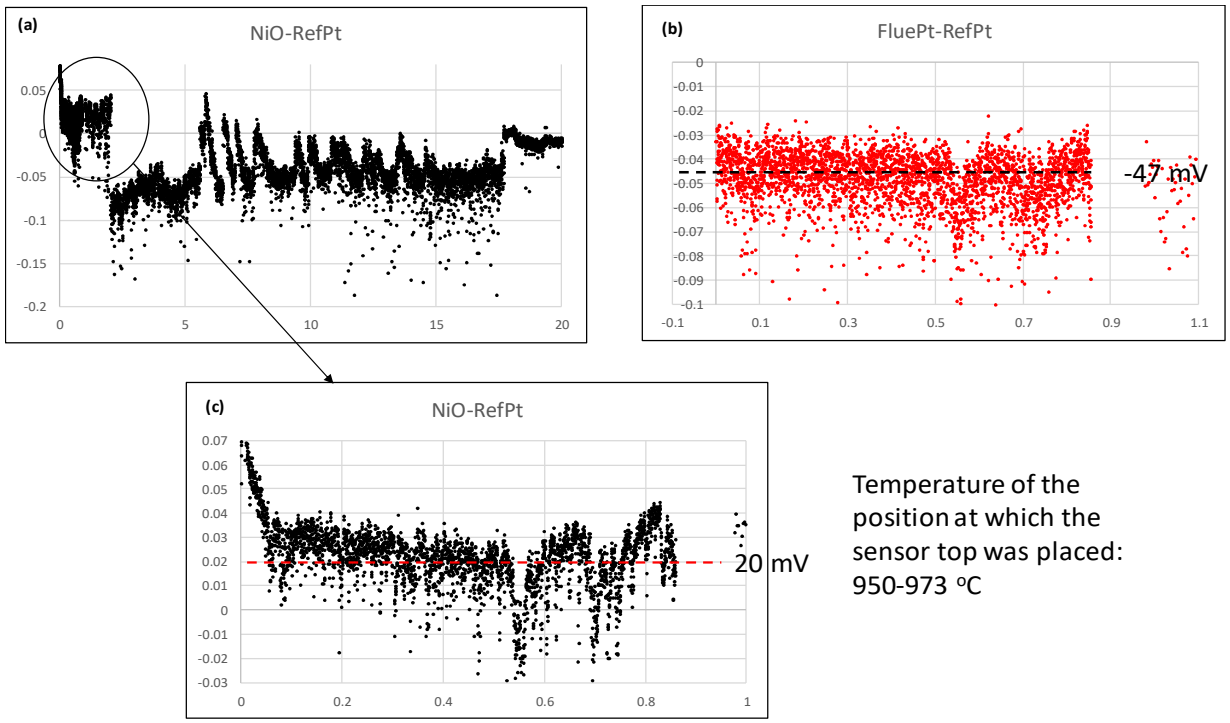

Figure. 51 Sensing test result of the designed sensor assembled in Longview's utility boiler. (a) potential difference between NiO electrode in the sensing side and RefPt electrode in the reference side, which is designed to measure the concentration of CO. (b) potential difference between FluePt electrode in the sensing side and RefPt electrode in the reference side, which is designed to measure the oxygen partial pressure. (c) Zoom-in on the data of the first hour (a).

First thing we need to look at is the signal of FluePt electrode as shown in Fig. 51 (b). Because Pt is a highly active electrode in high temperature, many kinds of gases such as hydrocarbons, CO and NO would be fully oxidized over the top surface of Pt. The only active gas arriving at the Pt/YSZ TPB interface is oxygen, therefore Pt is regarded as an excellent oxygen concentration sensor in high temperature. So what we get from Fig. 51(b) is the oxygen concentration in the boiler. After compared with the lab-testing data, -45 mV at around 1000 °C means 2.5%-3.5% PO_2. This value of oxygen concentration is in a good agreement with the reported value in the coal-fire power plant boiler.

Then what's worth noting is the data shown in Fig. 51(c), which would be the signal we assume coming from CO in the boiler. After comparing with the lab-scale data, if we use exponential correlation, 20 mV means 21607 ppm, which is not reasonable. If we use polynomial fitting for the lab-scale data the measured value of 20 mV corresponds to 2058 ppm CO. This value makes more sense. Actually, in the utility boiler system, there are many factors needed to be considered. Although we exclude the effect of CO_2 and some hydrocarbons, we still need to know how other gases affect, such as carbon-rich ashes, H_2S, SO_2, NO, NO_2 gases.

Fig. 52 shows images of the sensor after 20 h operation in the Longview's utility boiler. It is clearly seen that ashes covered the whole sensor top, indicating the extremely demanding condition in the boiler system.

Figure. 52 Images of the sensor after 20 h operation in the Longview's utility boiler.

Fig. 53 shows the 25-day sensing result at 8th floor of Longview's boiler. Unfortunately, we lost a lot of data of nearly 2 weeks because of the unexpected electricity shutdown at 8th floor twice in Longview. Thereby, although the sensor had been working, the data recording system was out of power.

At the beginning, the signal is positive, which is in agreement with the result of the last quarter indicating the effect of CO. However, gradually the signal is going negatively and reaches a large negative value of -0.3 V. This possibly means the CO effect is offset by other oxidizing reactions such as the burning of hydrocarbon. This also could mean a composition change of NiO, which leads to the loss of sensor sensitivity to CO. Fig. 54 show the sensor images after this near 1-month measurement. The dusts and ashes fully cover the sensor head. In fact, this dust coverage is thick, hard and stiff. More importantly, the sensing material NiO is nearly fully changed because the color of the NiO became yellow. At the end of the testing period, the reading is zero, and the connection is broken after examination. The platinum wires were found corroded severely after we took the sensor out.

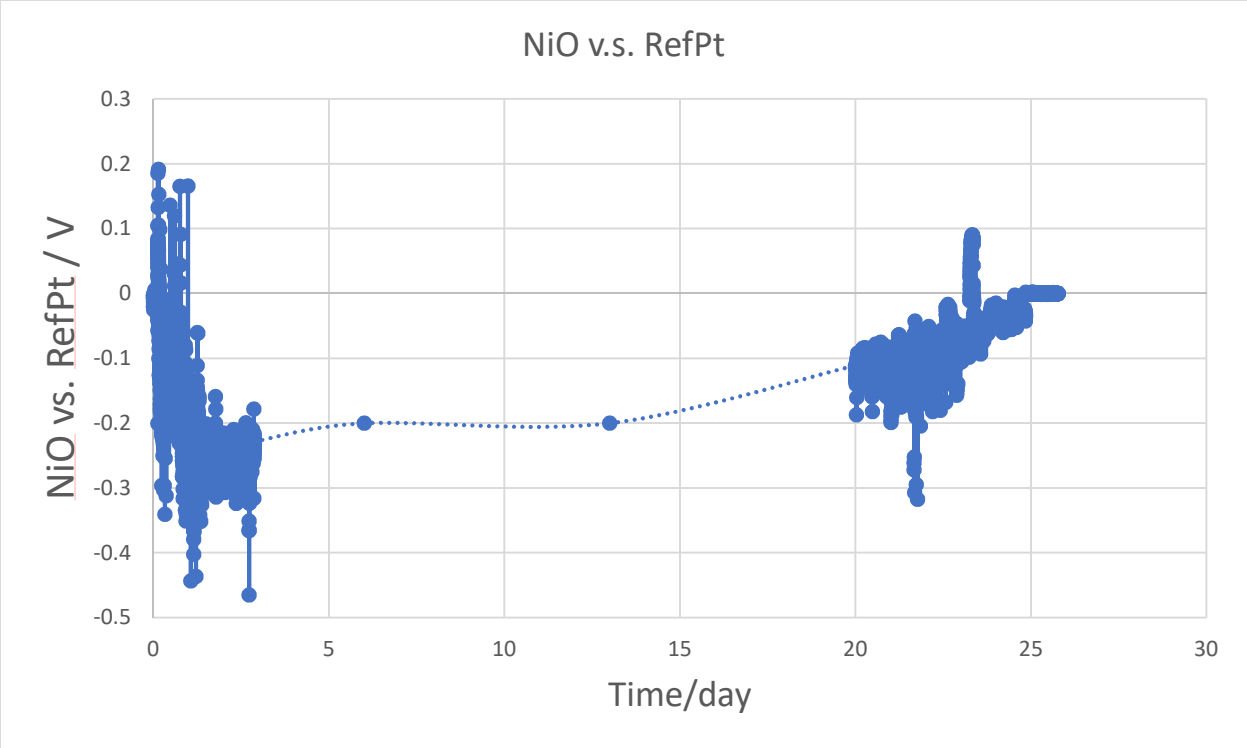

Figure. 53 25-day sensing result at 8th floor of Longview's boiler

Figure. 54 Sensor images after 25-day measurement

The 25-day infield measurement proves that the atmosphere in the boiler is extremely aggressive. Then we conducted our 3rd trial to increase the durability of the sensor. The whole sensor structure is similar to the previous one. But we changed the protective alumina tube to a stainless tube and

placed some porous refractory bricks on the top of the chamber to prevent the sensor materials from contacting the extreme poisoning ashes and dusts. The structure and images are shown in Fig. 55.

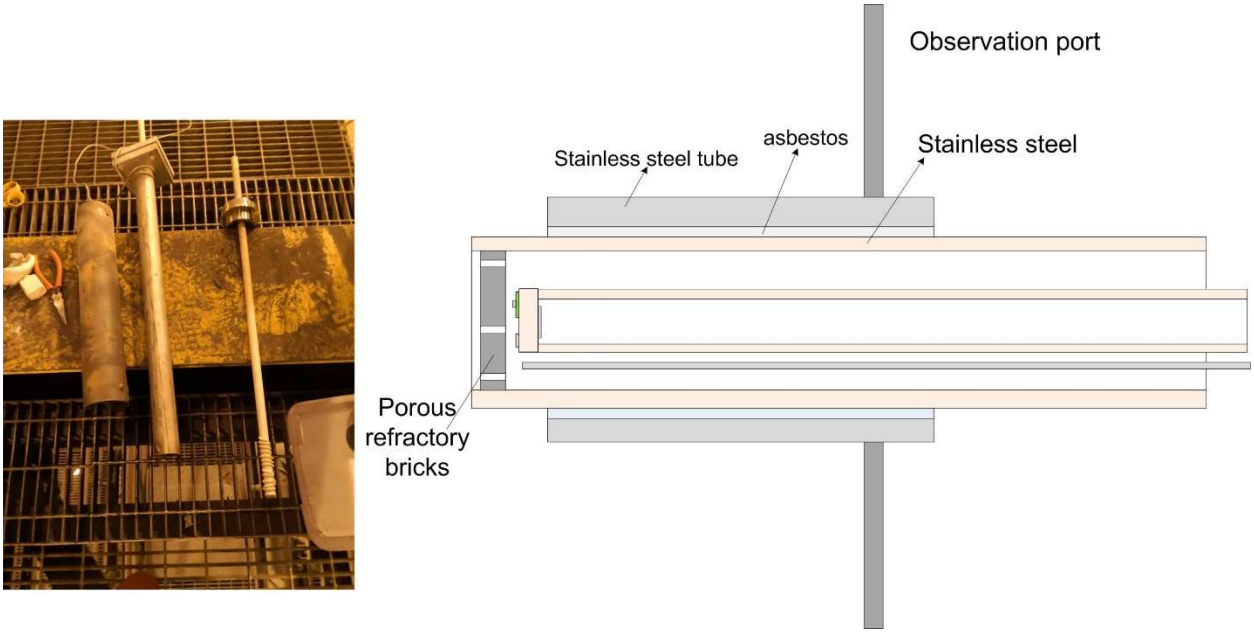

Figure. 55 Modified sensor structure for improved durability. A stainless steel tube and porous refractory bricks were used

Fig. 56 shows the 3rd trial 2-week data of the boiler test on the 8 floor. There is a large fluctuation of the signal. This may be due to the violent atmosphere change in the sensor chamber as the flue ash started to build up on the sensor shield. We suspect that the ashes and dusts blocked the porous structure of the porous refractory bricks eventually, preventing the gas exchange between the boiler and the sensor chamber.

2 weeks
930-950 C

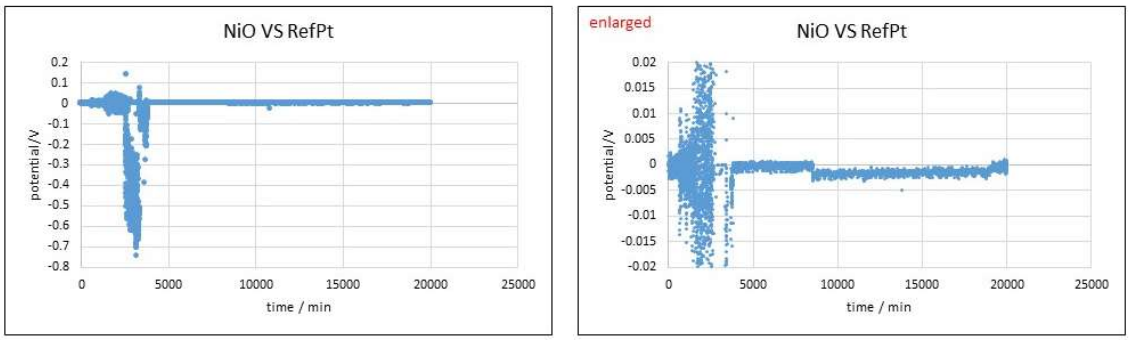

Figure. 56 the 2-week data of the boiler test on the 8th floor from a modified sensor structure.

3 CONCLUSIONS

This work found NiO a promising material for in-situ high temperature CO sensing in utility boilers, such as that in coal-fired power plants. Its characteristics of withdrawing high temperature as high as 1000 ºC and good sensitivity, selectivity and response time to CO make it an excellent candidate for being used in combustion monitoring sensors integrated into smart control system. Under the conditions of 0.5%-3% O_2 and 1000 ºC, the fabricated YSZ-based mixed potential sensor using porous NiO shows good sensitivity to ppm-scale CO, even having as high as 36 mV response to 1000 ppm CO. In addition, how the sample gas transport and NiO electrode's structure and geometry affecting the sensing behavior is studied. Results show that sensitivity can be improved by facilitating gas diffusion. Porous NiO has higher sensitivity to CO than dense NiO, but at meantime, the porous structure results in much higher response time. Selectivity tests on the effects of CO_2, CH_4 and steam on CO sensing were also conducted. NiO is insensitive to even 10% CO_2. CH_4 doesn't shift the average value of CO sensing response, however it makes the sensing process unstable due to the enlarged signal fluctuation. 2% Steam exerts a great influence on NiO's sensing. Porous NiO electrode doesn't show obvious variations with the CO content changing from 100 ppm to 1000 ppm. In contrast, the sensitivity of porous NiO electrode to low CO range of 0-100 ppm is enhanced significantly. This may be due to the decreased number of available adsorption site for CO, which is occupied by H_2O-related species, making the CO-related absorbates saturated when CO content is higher than 100 ppm. It's worth noting that the potential of NiO exhibits positive relationship with CO content. This is opposite to nearly all reported results in the works of mixed potential sensors to CO. We found it might be due to the electrochemical reduction of CO during the interaction with NiO at 1000 ºC rather than being oxidized.

Finally, because of the great potential of our NiO electrode, we managed to incorporate this sensor into a novel sensor test station in the coal-fired boiler at Longview Power LLC., Longview operates one the U.S.'s newest and cleanest coal-fired boilers, an Amec Foster Wheeler first-of-a-kind, once-through, low-mass flux, vertical tube Advanced Supercritical Boiler producing 700 MW of electricity. Our testing results shows the effectiveness of our gas sensor to provide real-time CO and O2 sensing, and the need to improve the sensor packaging & accessories to improve the long-term stability in real operation conditions.

4 FUTURE WORK

1) Improving packaging of the sensor to improve the long-term stability of it in the harsh coal-fired boiler environment
2) Conducting more field test in utility boilers if possible, to obtain more data about the sensitivity and stability of the developed sensor and to optimize the sensor design.
3) More mechanistic research work on the interactions between CO and NiO.